



Effects of seasonal cycle fluctuations in an A1B scenario over the Euro-Mediterranean region

Alessandro Dell'Aquila, Sandro Calmanti*, Paolo Ruti, Maria Vittoria Struglia, Giovanna Pisacane, Adriana Carillo, Gianmaria Sannino

Italian National Agency for New Technologies, Energy and Sustainable Economic Development (ENEA), Energy & Environment Modeling Unit Climate & Impact Modeling Laboratory (UTMEA-CLIM), CR Casaccia, Via Anguillarese 30, 100123 Santa Maria di Galeria, Rome, Italy

ABSTRACT: We analysed the downscaling of an A1B scenario simulation for the Euro-Mediterranean area performed with a regional earth system model by focusing on long-term variations in the seasonal cycle of key impact indicators (surface temperature, hydrological cycle). The output of the regional model was compared with the driving global simulation (ECHAM5/MPI-OM) and with available observations. Our objective was to highlight the potential additional information end-users may access by using a high-resolution regional coupled system in place of the corresponding coarser global driver. In the regional downscaling, the large sea surface temperature (SST) bias simulated by the global driver is partially reduced, and SST spatial patterns are in better agreement with those observed in the reference climatology, thereby supporting the tenet that coupling the atmosphere with a high-resolution interactive ocean over small areas characterized by complex orography may improve specific aspects of regional climate modelling. A more accurate description of orography produces in the regional model a narrower identification of the effects of a warmer climate on intense precipitation events and on other key environmental indicators, such as the extension of snow cover and the aridity index. An example of the effect of climate variability on river discharge is also presented for a medium/small catchment basin in northern Italy, the Po River, which responds both to variations in rainfall rates and to the amount of snowfall over the Alps. In contrast with the gross underestimation of the global driver, regional simulation produces a reasonable estimate of the observed average discharge ($1500 \text{ m}^3 \text{ s}^{-1}$) and of its seasonal variability, which provides a reliable baseline for societal impact studies.

KEY WORDS: Mediterranean · Regional climate · Scenario · Sea surface temperature · Hydrological cycle

Resale or republication not permitted without written consent of the publisher

1. INTRODUCTION

Scenarios of stabilized CO_2 concentration above 400 ppm are very likely to produce sizeable changes in rainfall patterns in the Euro-Mediterranean region, and temperature fluctuations that are beyond the range recorded during the last few centuries (Giorgi et al. 2004, Déqué et al. 2005). In a warming scenario, the northward shift of mid-latitude flow regimes implies a decreasing trend in precipitation over the Euro-Mediterranean region and altered inter-annual and intra-seasonal variability (Ulbrich et

al. 2009). In particular, the potential drying of the Euro-Mediterranean region has been attributed to a northward shift of the Atlantic storm track, which induces more stable atmospheric conditions, especially during summer (Giorgi & Lionello 2008).

Sanchez-Gomez et al. (2009) presented a comprehensive study of the projected long-term fluctuations in the hydrological cycle over the Euro-Mediterranean region, based on the scenario simulations produced during the EU project ENSEMBLES. Their multi-model evaluation shows that, compared to the present freshwater deficit of about 1 m yr^{-1} (Mariotti et

al. 2002), increasing evaporation along with decreasing rainfall, decreasing river discharge and Black Sea input may lead to an additional freshwater deficit of 40% over the Euro-Mediterranean region during the next century.

The Euro-Mediterranean region is characterized by extremely complex coastlines and topographical features, such as the Alpine, Apennine, Pyrenees and Balkan mountain chains, the Italian and Hellenic peninsulas and many large islands. The complex orography and the peculiar geometry of the ocean basin are important drivers for the local phenomena that characterize Mediterranean climate, such as lee cyclogenesis (Trigo et al. 2002) and deep water formation (Millot 1999, Roether et al. 1996). Therefore, reliable projections of climate variability over the Euro-Mediterranean region must necessarily rely on the use of suitable regionalization techniques. However, state-of-the-art global climate models adopted for global impact studies and policy planning have a resolution that is far too coarse to correctly describe air–sea exchanges (in particular the latent heat flux) and their variability within the Euro-Mediterranean region (Elguindi et al. 2009). By running a regional climate model over the Mediterranean region, Somot et al. (2008) observed an amplification of the climatic signal with respect to analogous simulations performed with atmosphere-only models. This result was attributed to the higher consistency between the high-resolution sea surface temperature (SST) field, the predicted energy fluxes at the atmosphere–ocean interface and the vertical structure of the atmosphere. The PROTHEUS regional earth system described and validated by Artale et al. (2010) represents another significant step in the direction of responding to the challenge of producing reliable climate scenarios for the Mediterranean basin. In the coupled PROTHEUS system, the atmospheric model is forced at the surface by a high-resolution interactive ocean model, the SST of which responds, in turn, to mesoscale circulation patterns produced by the regional atmospheric model. A key improvement of this modelling tool is the ability to produce realistic high-resolution SST and wind speed, which results in a more reliable description of heat and water fluxes and of feedbacks between the atmosphere and ocean models.

In the present study we compare the outcome of the PROTHEUS regional earth system model with those obtained from its driving global model over the Euro-Mediterranean region, in terms of the prevailing seasonal cycle of key environmental parameters and the large deviations from it. Specific regard is paid to the representation of the hydrological cycle.

Moreover, to provide a baseline for future comparisons in the broader context of water resource management, we analyse key impact indicators, such as the frequency of intense rainfall events, the aridity index and snow cover, which are likely to be affected by the improvements implied in the adoption of regional models as tools for impact studies.

The paper is organized as follows: Section 2 describes the model configuration and the simulations considered for the analysis. In Section 3 we compare the mean differences in the seasonal cycles of key variables affecting the hydrological cycle, as produced by the PROTHEUS model and by its global driver ECHAM5/MPI-OM, both under present and future climate conditions over the Euro-Mediterranean region. In Section 4 we analyse the A1B scenario from the point of view of some critical impact parameters; we draw our conclusions in Section 5.

2. SIMULATIONS

2.1. Models

The PROTHEUS system is comprised of the RegCM3 atmospheric regional model and the MITgcm ocean model. For a complete description of the coupled system the reader is referred to Artale et al. (2010). The coupling of RegCM3 and MITgcm is done with the OASIS3 coupler (Valcke & Redler 2006), which enables both the synchronization of the 2 models and the interpolation of coupling fields from the source to the target grid. Every 6 h, the ocean model receives the wind stress components, as well as the total heat and freshwater fluxes from the atmosphere. In the same intervals, the atmospheric model updates the SST patterns with those produced by the ocean model. No additional term is applied to obtain a relaxation of the model towards the observed climatology.

In the following, we briefly review the main characteristics of the 2 models to emphasize the improvements over the configuration used in Artale et al. (2010). RegCM3 is a 3-dimensional, sigma-coordinate, primitive equation, hydrostatic regional climate model. A detailed description can be found in Giorgi et al. (1993a,b). Successive upgrades have been described by Giorgi & Mearns (1999) and Pal et al. (2007). The model configuration adopted for the present study has a uniform horizontal grid spacing of 30 km on a Lambert conformal projection and 18 σ -levels. The simulation is performed for an area ranging from 20 to 60°N over the entire Mediterranean Sea (Fig. 1a). Lateral boundary conditions are

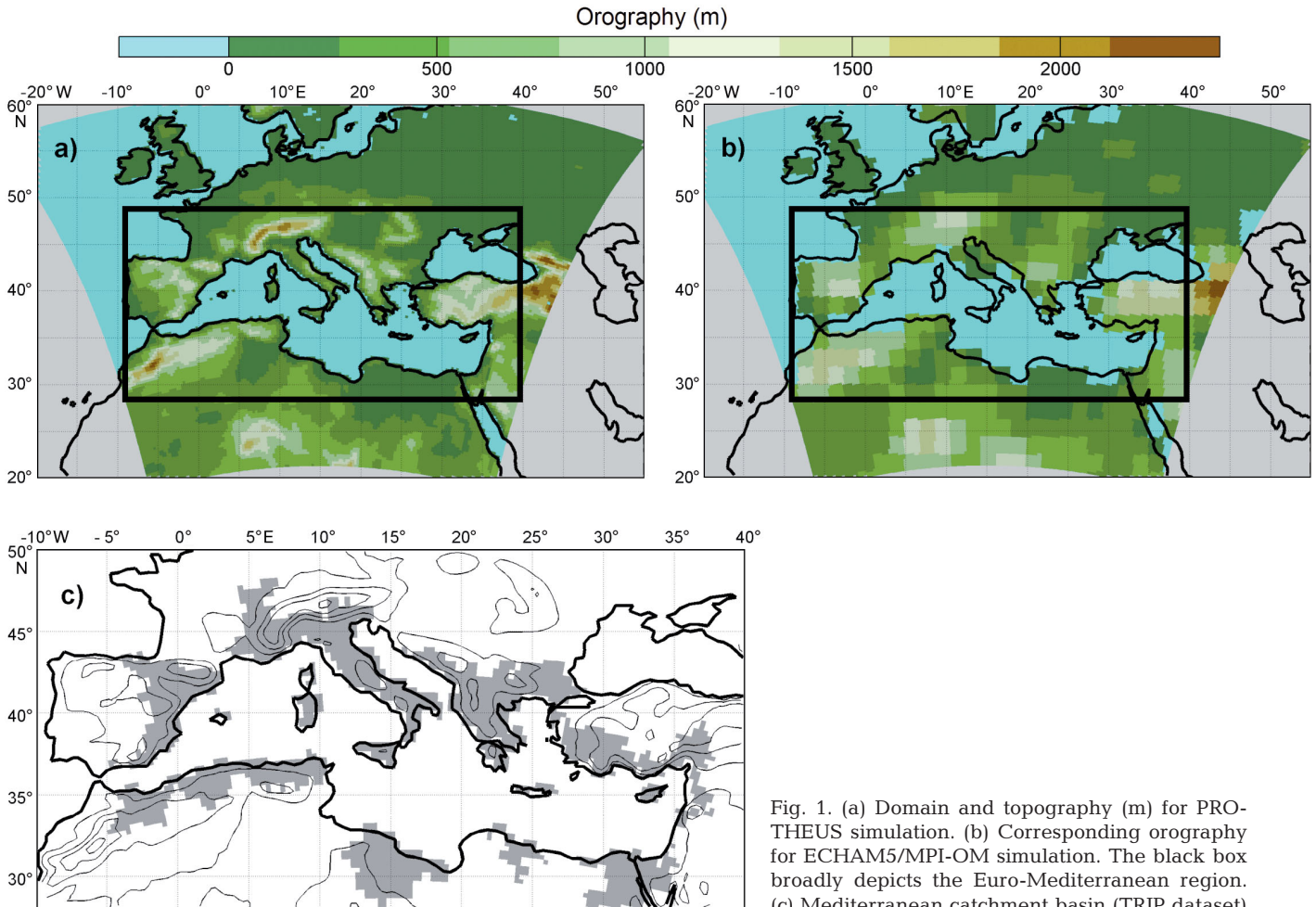


Fig. 1. (a) Domain and topography (m) for PROTHEUS simulation. (b) Corresponding orography for ECHAM5/MPI-OM simulation. The black box broadly depicts the Euro-Mediterranean region. (c) Mediterranean catchment basin (TRIP dataset)

supplied every 6 h by interpolating horizontal wind components, temperature, specific humidity and surface pressure from the driving global atmospheric model.

The ocean component is based on the Mediterranean Sea model by Sannino et al. (2009). It is characterized by a horizontal resolution of $1/8^\circ \times 1/8^\circ$, equivalent to rectangular meshes of variable resolution with a meridional side of about 14 km and a zonal side ranging from about 9 km in the northern part of the domain to about 12 km in the southern part. The model has 42 vertical Z-levels, with a resolution varying from 10 m at the surface to 300 m in the deepest part of the basin and an intermediate resolution of about 40–50 m between the depths of 200 and 700 m. The performance of the oceanic component of the PROTHEUS system in reproducing Mediterranean circulation has been discussed by Sannino et al. (2009). In particular, the configuration adopted for the present study corresponds to the NOGR configuration, characterized by an explicit

(although at relatively low resolution) description of the Strait of Gibraltar. In particular, we use natural boundary conditions for salinity, i.e. precipitation, runoff and evaporation are treated as acting on the total volume of freshwater.

With respect to the simulations described by Artale et al. (2010), we substituted the observational monthly climatological river discharge dataset with monthly river discharges interactively computed from the RegCM3 total runoff.

River discharge is calculated by spatially integrating the simulated monthly mean total runoff over a large portion of the catchment basin. The integration is based on the total runoff integrated pathway (TRIP) dataset, which maps the land–water flow directions onto a $0.5^\circ \times 0.5^\circ$ regular global grid (Oki & Sud 1998). By following the TRIP classification, we identify 148 river mouths discharging into the Mediterranean Sea (Fig. 1c) and 50 river mouths discharging into the Black Sea. To derive a realistic estimate of the freshwater flux that reaches the

Mediterranean Sea from the Black Sea through the Dardanelles Strait, the value for the total discharge into the Black Sea is rescaled (runtime) using coefficients computed from a preliminary stand-alone simulation in which the atmospheric model is driven by the ERA40 reanalysis. We derive the rescaling coefficient from the optimal linear fit with the Stanev climatology (Stanev et al. 2000). The rescaled water flux is then treated as a single river mouth for the Aegean Sea. The effect of the rescaling is to reduce the total discharge into the interior of the Black Sea, with a larger impact during winter.

The configuration of the global driver ECHAM5/MPI-OM is that adopted for the AR4 IPCC runs in the CMIP3 database (Marsland et al. 2003, Roeckner et al. 2003). The global atmospheric component (ECHAM5) is run at a spectral resolution of T63, corresponding to approximately 200 km at mid-latitudes, and has 32 vertical levels. All the details on the atmospheric configuration have been reported by Roeckner et al. (2003). The topography over the Euro-Mediterranean region is compared to the corresponding PROTHEUS topography in Fig. 1b, showing that important topographic features such as the Alps and the Pyrenees are missing in the global driver. A mass-flux-modified scheme is adopted for shallow, mid-level and deep convection (Tiedtke 1989). The land hydrological model also includes a river routing scheme at a resolution of 0.5° (Hagemann & Dümenil Gates 2001). The oceanic component (MPI-OM) has a resolution of 1.5° , with a conformal mapping grid using poles over Greenland and Antarctica and 40 vertical levels (Marsland et al. 2003). This model configuration results in poor representation of Mediterranean Sea circulation, with, for example, no explicit connection to the Atlantic Ocean.

2.2. Global drivers and regional downscaling

We performed a single regional scenario simulation for the period 1951–2050 driven by the ECHAM5/MPI-OM simulation identified as *run3* in the CMIP3 database (www-pcmdi.llnl.gov). For the period 1951–2000, the global driver uses the observed greenhouse gas (GHG) concentration values as adopted for the 4th IPCC Assessment; for the period 2001–2050, GHG concentrations follow the SRES A1B scenario. The same GHG concentrations were applied to regional downscaling. We will refer to the 1950–2000 PROTHEUS simulation as P_20C, and to the 2001–2050 PROTHEUS simulation, as P_A1B. The corresponding global drivers will be named E_20C and E_A1B.

Previous assessments of ECHAM5/MPI-OM performance have been conducted in the context of global model inter-comparison studies. For example, the ability of the model to describe the El Niño/Southern Oscillation (ENSO) and tropical variability has been analysed by Van Oldenborgh et al. (2005), Jungclaus et al. (2006) and Ruti & Dell'Aquila (2010), while its capacity for representing extra-tropical climate is discussed by Van Ulden & van Oldenborgh (2006) and Bengtsson et al. (2006). Its ability to produce correct representation of Atlantic storm tracks has also been the subject of a recent study by Ulbrich et al. (2009), who adopted a 2–6 d band-pass filter and showed that the 500 hPa simulated in E_20C has the best correlation of storm track pattern with the ensemble mean, and correctly places the centre of action of the storm track in the Atlantic. On the other hand, Lucarini et al. (2007) analysed the standing and travelling components of mid-latitude atmospheric regimes and showed that E_20C is one of the model simulations that tends to show the largest overestimation of mid-latitude synoptic activity. As the Mediterranean climate is highly sensitive to Atlantic storm tracks and to ultra-long planetary waves, our simulation will benefit from the correct placement of the synoptic mid-latitude disturbances, although the global bias in their amplitude might affect our results as it propagates across the boundaries.

As for the oceanic component, the driving simulation E_20C underestimates salinity and temperature by about 0.5 psu and 1°C , respectively, in the upper layers of the Gulf of Cadiz, with respect to the climatology of Levitus (1982). Test simulations show that this systematic bias affects the explicit water mass exchange through the Strait of Gibraltar and the resulting Mediterranean thermohaline circulation, in line with the results presented by Sannino et al. (2009). Therefore, we decided to prescribe the monthly Levitus climatology as the oceanic boundary condition for P_20C and to apply monthly temperature and salinity anomalies from E_A1B (with respect to E_20C) to the Levitus baseline in the scenario simulation. The initial conditions for the ocean model are derived from a stand-alone ocean simulation, in which the 3-dimensional temperature and salinity data were relaxed towards MEDATLAS II (MEDAR Group 2002) climatology, with a relaxation coefficient of 5 d. The model was run under a perpetual year surface forcing, and the velocity field was left free to evolve until the 3-dimensional integrated kinetic energy over the entire domain reached a stable value.

We analyse the simulations P_20C and P_A1B and the corresponding driving scenarios E_20C and

E_A1B by focusing on the domain adopted by Mariotti et al. (2002) and shown in Fig. 1, which spans the area 10°W–40°E and 28–47°N. A general overview of the main properties of the simulations considered in our analysis (i.e. surface temperature ts , precipitation pr , evaporation et) is reported in Fig. 2, and the main statistics are summarized in Table 1. We treat sea- and land-grid points separately in order to identify potential improvements led to by the adoption of an ocean–atmosphere coupled model.

2.3. Overview of the scenarios

The evolution of SSTs and the comparison with reference observations (Fig. 2a) show that the regional coupled model produces a partial correction of the large cold bias simulated by the global driver. Compared to the reference GISST observational dataset provided by Rayner et al. (2006), the bias is reduced from $>1.5^\circ\text{C}$ in the E_20C to slightly $<1^\circ\text{C}$ in P_20C. There is no observational input to the simulations in Fig. 2, except for the Levitus climatology (and associated anomalies) as a boundary condition to the Atlantic box of the oceanic component; the bias reduction observed in the surface temperatures of the Mediterranean Sea is comparable to the correction imposed in the Atlantic box to the signal originating from the global driver. Therefore, the strategy of adopting a realistic (i.e. de-biased) Atlantic inflow seems a key ingredient for obtaining reliable down-scaling.

The most important improvement related to the adoption of an ocean–atmosphere coupled modelling approach is illustrated in Fig. 3, where we compare the summer SST patterns of P_20C and E_20C with the corresponding GISST data. The meridional SST gradient, mainly over the eastern Mediterranean basin, is well reproduced in P_20C, whereas, in E_20C, the SSTs are colder and spatially more homogeneous. For example, the summer warm pool in the Ionian Sea, which is not present at all in E_20C, is well depicted in P_20C.

The regional simulations are generally characterized by heavier precipitation (Fig. 2c,d). We have also reported in Fig. 2d the observed rainfall over land provided by New et al. (2002), which confirms the systematic tendency of PROTHEUS to overestimate rainfall over steep topography (Artale et al. 2010). On the other hand, the global simulations underestimate strong rainfall over land. Table 1 also indicates a statistically significant, albeit small, negative trend in precipitation over land. Over sea, the

trend in the regional simulations is not statistically significant, whereas, in the global simulations, a very weak downward trend is detected. In summary, although we target a different time horizon, the modelled tendencies reflect the same trends as those discussed by Mariotti et al. (2008) and Sanchez-Gomez et al. (2009).

The regional simulations are also characterized by higher evaporation fluxes (Fig. 2e,f) compared to the reference OAFUX dataset (Yu et al. 2008). A slight positive trend is observed over the sea, likely due to warming. In contrast, no significant trend of evaporation can be detected over land.

The OAFUX evaporation dataset closely matches the long-term variability of the observed SST. The same agreement between SST and evaporation is not observed in the models. Such a deviation in behaviour may be attributed to major deficiencies in the formulation of models for surface processes. However, the possibility that remotely sensed evaporation is too biased towards surface temperature retrievals cannot be ruled out and should be investigated in more detail.

3. SEASONAL CYCLES

We compare our regional downscaling to the global driver by considering atmospheric variables that are relevant to the hydrological budget. The seasonal cycles for the variables of interest are computed as spatial and temporal averages, such that:

$$\overline{Q_{(i2-i1)}(k)} = \frac{1}{N(i2-i1+1)} \sum_{i=i1}^{i2} \sum_l Q_{il}(k) \quad (1)$$

where k runs over all time steps in 1 model year, i runs over a selected range of years in the simulation and l runs over either the land or the sea N grid points of each model land–sea mask. The standard deviation of $Q_i(k)$ at each time k during the year, $\sigma(Q(k))$, is also considered as a measure of the inter-annual variability of the seasonal cycle. To fully characterize the variability of the seasonal cycle we also compute the intra-seasonal deviations from the reference seasonal cycle, such that:

$$Q'_i(k) = \sum_l Q_{il}(k) - \overline{Q_{(i2-i1)}(k)} \quad (2)$$

To illustrate the potential long-term fluctuations in the seasonal cycle, the 3 quantities $\overline{Q_{(i2-i1)}(k)}$, $\sigma(Q(k))$ and the distribution of Q'_i are shown in Figs. 4–7, for the periods 1961–1970 (20C, blue lines) and 2041–2050 (A1B, red lines), whereby the upper panels

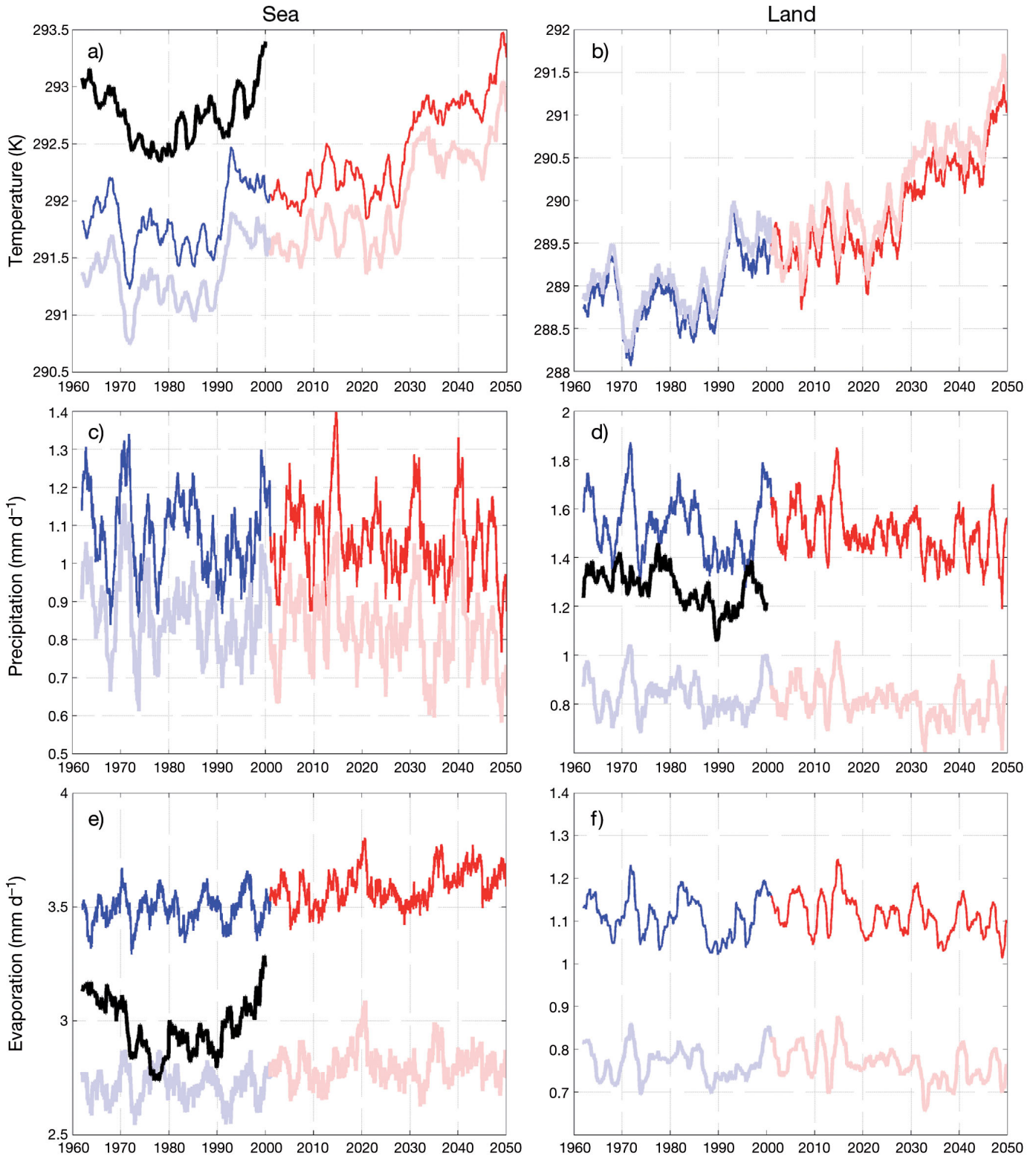


Fig. 2. Time series (dark red/blue lines) averaged over sea and over land of: (a,b) surface temperature t_s , (c,d) daily rainfall pr and (e,f) evaporation et . The blue lines represent the P_20C period and the red lines represent the P_A1B period, both for 2041–2050. Centered yearly running mean smoothing was applied to all data displayed in the panels. The black lines correspond to observational datasets (when available). The temporal behaviour reproduced in the global driver ECHAM5/MPI-OM is reported as lightly shaded red/blue lines corresponding to the period above. See Section 2.3 for further details

Table 1. Means (\pm SD) and trends for surface temperature, daily rainfall and evaporation, averaged over sea and land. To filter out the seasonal cycle centered yearly running mean smoothing is applied to all data (see Fig. 2). The trends are computed from the annual means, and they are statistically significant at the 95% confidence level (Mann-Kendall test). To compute the standard deviation we consider detrended time. Dash: no significant trend

	Temperature (K)		Precipitation (mm d ⁻¹)		Evaporation (mm d ⁻¹)		Water budget (mm yr ⁻¹)
	Sea	Land	Sea	Land	Sea	Land	
PROTHEUS							
20C	291.8 \pm 0.3	288.9 \pm 0.3	1.1 \pm 0.1	1.53 \pm 0.07	3.49 \pm 0.07	1.11 \pm 0.05	559 \pm 77
A1B	292.5 \pm 0.2	289.9 \pm 0.3	1.0 \pm 0.1	1.49 \pm 0.09	3.59 \pm 0.07	1.11 \pm 0.04	606 \pm 62
Trend (decade ⁻¹)	0.16	0.26	–	–0.01	0.02	–	12
ECHAM5/MPI-OM							
20C	291.3 \pm 0.2	289.1 \pm 0.3	0.86 \pm 0.09	0.83 \pm 0.07	2.71 \pm 0.07	0.77 \pm 0.04	615 \pm 43
A1B	292 \pm 0.2	290.1 \pm 0.3	0.82 \pm 0.09	0.81 \pm 0.07	2.80 \pm 0.07	0.76 \pm 0.03	664 \pm 46
Trend (decade ⁻¹)	0.16	0.26	–0.01	–0.008	–	–	12

refer to sea-grid points and the lower panels refer to land-grid points. The time series reported in Fig. 2 show that the time intervals considered for the analysis (1961–1970 and 2041–2050) have a difference in averaged surface temperatures of $>1^\circ\text{C}$, compared to a significantly smaller variability on a decadal time scale (Fig. 2a,b, Table 1). We are considering a system that is in a transient state; thus, in selecting reference time intervals for our analysis, we need to find a compromise between the need for sufficient samples to support good statistics (e.g. the 30 yr required for a formal definition of climate) and the need to compare time intervals that are internally homogeneous and coherent. Therefore, we consider the 10 yr time slice to be relevant for our analysis. For the sake of completeness, we have also performed the analysis discussed in this section for the intervals 1961–1980 and 2031–2050, and we obtained similar results (not shown).

The panels on the left (a and c) summarize a fairly complete set of information concerning the mean seasonal cycle of the selected variables and the corresponding range of variability produced by regional downscaling and the global driver. The variability is reported by emphasizing a range of $\pm\sigma(Q(k))$ around the mean. To smooth the seasonal cycle, we apply a centred 11 d running mean. The range of variability produced with the global driver ECHAM5/MPI-OM is also reported (light shading, with blue and red corresponding to the 20C and A1B period, respectively). Light purple shading corresponds to an overlap in the variability of E_20C and E_A1B. The panels to the right (b and d) show the probability density functions (PDFs) of Q'_i over land and over sea, for both regional downscaling (solid lines) and the global driver (light shading). In the figures we also report the results of Kolmogorov-Smirnov (KS) tests for the null hypothe-

sis that the PDFs extracted from P_A1B and P_20C are equal. KS = 1 indicates the case in which the null hypothesis can be rejected at the 99% confidence level; KS = 0 indicates that the null hypothesis cannot be rejected.

3.1. Temperature (*ts*)

A remarkable characteristic of the coupled PROTHEUS model is the possibility of generating high-resolution SST that are coherent with the high-frequency and fine-scale variability of observed SSTs (Artale et al. 2010). This characteristic of the PROTHEUS model is expected to improve the projections of SST over the standard capabilities of coarser global models. In Fig. 4a, we compare the modelled seasonal cycle of SSTs to the reference seasonal cycle extracted from the GISST dataset. We highlight a few key discrepancies between regional downscaling and the global driver. During summer, the phase of maximum SST is anticipated to be around 1 mo earlier with PROTHEUS (beginning of August) than with ECHAM5/MPI-OM (beginning of September), with the PROTHEUS phasing closer to the GISST observational reference. Furthermore, no significant spatial patterns emerge in the comparison between the projected future time slices, P_A1B and E_A1B, and the corresponding present climate, P_20C and E_20C (not shown). Therefore, the improvements described in Section 2 in the representation of the meridional gradient and in the spatial patterns of SSTs are propagated in the model scenarios, regardless of the overall warming observed in the Mediterranean. These characteristics of coupled regional models are of particular relevance for the production of climate scenarios, because any

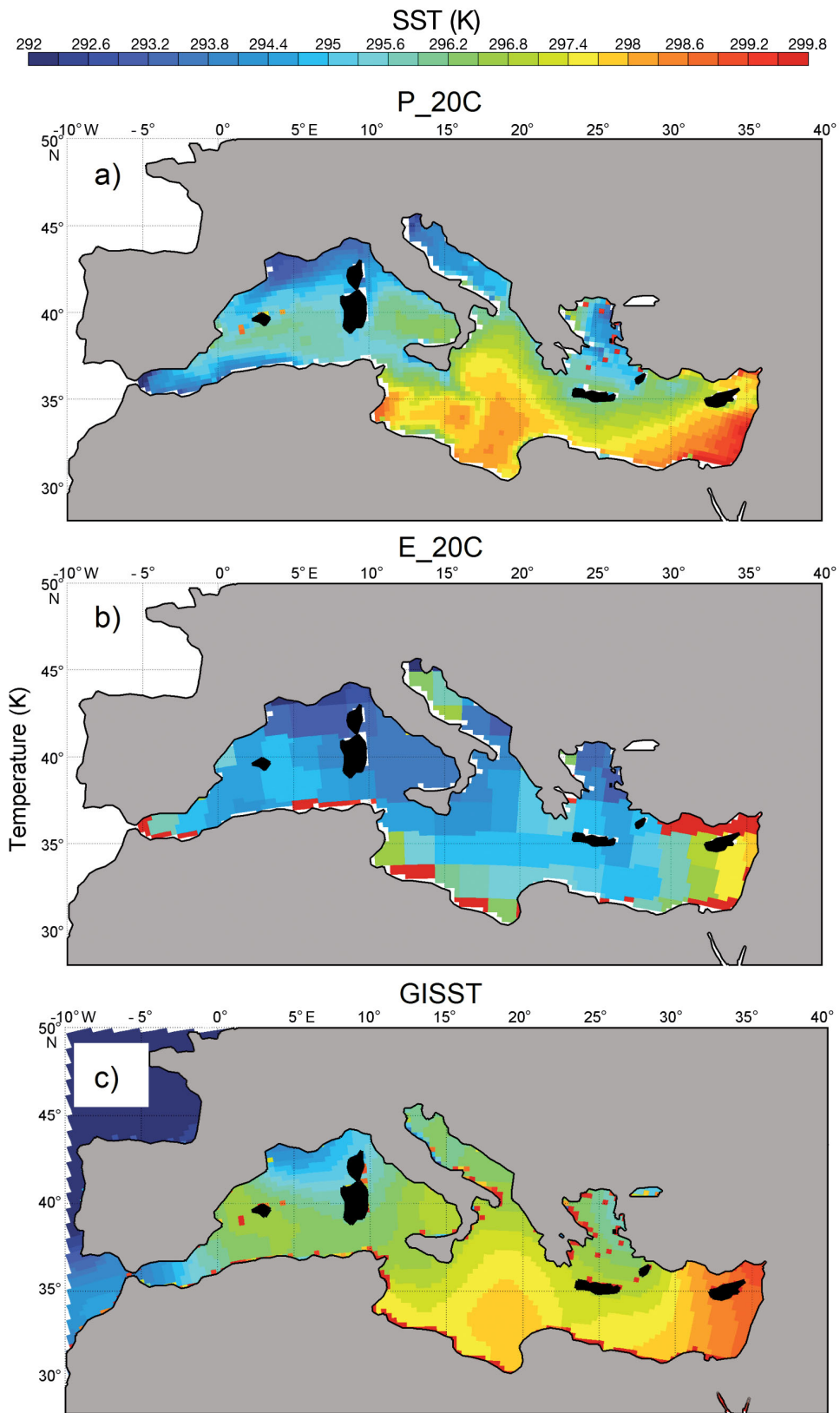


Fig. 3. Seasonal (June, July, August) sea surface temperature (SST) average in the PROTHEUS (P_20C) and ECHAM5/MPI-OM (E_20C) simulations and in the GISST dataset. The global driver and GISST patterns are reported on the PROTHEUS grid

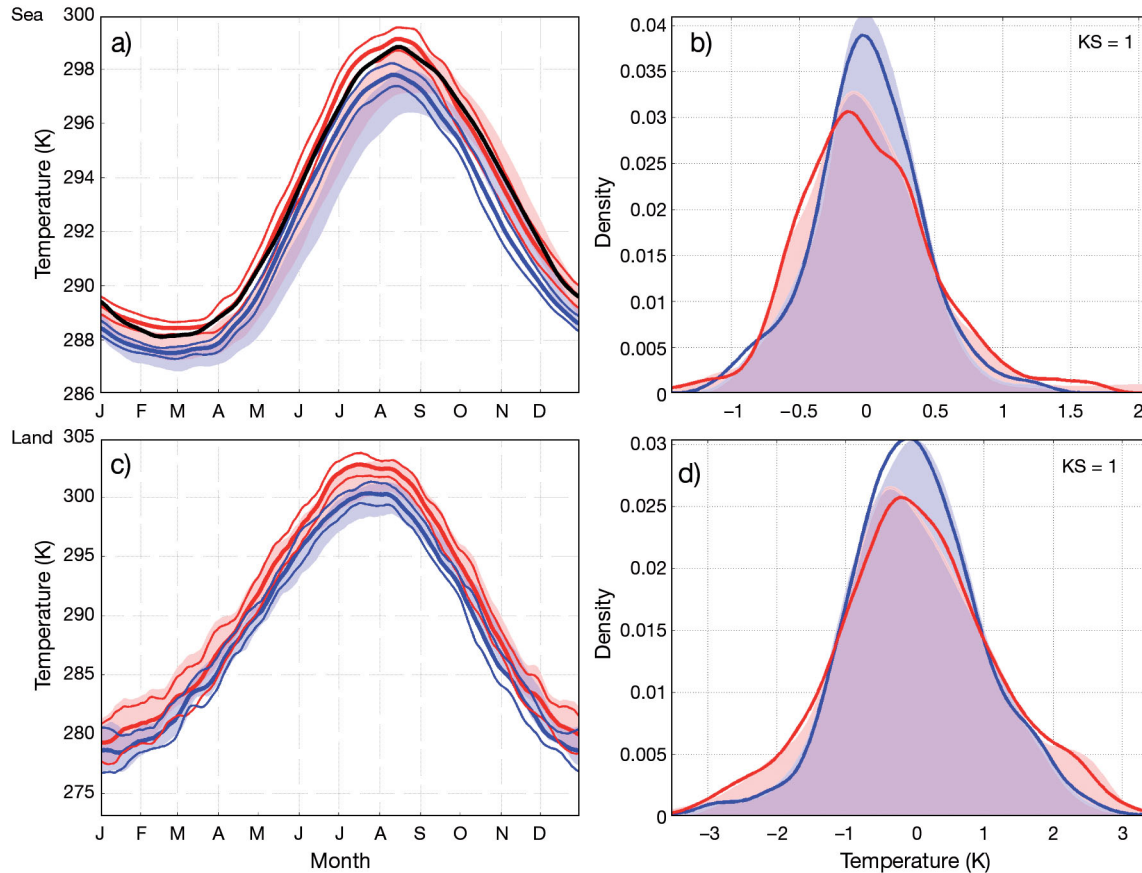


Fig. 4. Average seasonal cycle of surface temperature (ts) over (a) sea and (c) land. The blue line represents the reference 20C period (1961–1970); the red line represents the A1B period (2041–2050). Left panels: thick lines mark the average seasonal cycle \bar{ts} and thin lines mark $\pm\sigma(ts \cdot k+)$ above or below the mean. Centered 5 d running mean smoothing was applied to all data displayed in the panels. The black line is the average seasonal cycle of the GISST dataset. Right panels: The range of variability produced with the global driver ECHAM5/MPI-OM is also reported as lightly shaded regions in red and blue corresponding to the periods above. The overlapping region E_20C/E_A1B is a darker purple colour. Distribution of the deviations of ts' from the average seasonal cycle \bar{ts} over (b) sea and (d) land. Colour codes are the same as for the left panels. PDFs were computed by adopting a kernel function estimator and by using a window parameter $h = 3.5 \times \Delta$, where Δ is the bin amplitude. We assume 100 bins in the interval between the minimum and maximum deviations. If the Kolmogorov-Smirnov test (KS) = 1, the differences in the deviations ts' between P_20C and P_A1B from the reference seasonal cycle are significant at the 99% confidence level by using a Kolmogorov-Smirnov test (KS = 0 otherwise)

improvement in the description of SSTs may have an impact on local processes, such as cyclogenesis and deep convection, that are affected by the presence of specific temperature thresholds and patterns.

Significant differences exist between the behaviours of the global driver and of regional downscaling from a point of view of the long-term fluctuations in the basin-averaged SST seasonal cycle. In the case of regional downscaling, the deviations between P_A1B and P_20C in the seasonal cycle of SSTs exceed the amplitude of inter-annual variability during almost the entire seasonal cycle (Fig. 4a). On the other hand, in the case of E_20C and E_A1B, there is significant overlap (purple shaded) in the ranges of likely fluctuations of SSTs, especially during summer. This in-

dicates that downscaling tends to amplify the climatic fluctuations in the seasonal cycle of SSTs with respect to those produced by the global driver.

The distributions of the deviations ts' from the prevailing seasonal cycle for the global driver also show sizeable differences. In particular, with respect to cold anomalies, events of intermediate intensity (around -1°C averaged over the entire basin) tend to be slightly more frequent with the global driver (E_A1B) than with the corresponding downscaling (P_A1B). Note that a stand-alone atmospheric-only configuration of the regional model would not show any difference with respect to the global driver. In fact, a stand-alone configuration of the atmospheric component would usually be driven at the sea surface by

the same SSTs produced with the global driver. In contrast, with respect to warm anomalies, the global driver and regional downscaling tend to exhibit similar behaviour. In particular, large warm deviations from the reference seasonal cycle (Fig. 4b) tend to increase in scenario P_A1B, where the tails of the distributions are more densely populated. The existence of significant differences in the deviations ts' between P_20C and P_A1B from the reference seasonal cycle is also confirmed by a KS test at the 99% confidence level.

Over land we also obtain an overall warming trend for the modelled future scenario, both with downscaling and the global driver. In the comparison between P_20C and P_A1B, the differences exceed the corresponding inter-annual variability only during summer (Fig. 4c). In comparison, with the global driver, the differences between E_20C and E_A1B always remain within the range of inter-annual variability. Over land, the frequency of the large deviations ts' from the reference seasonal cycle (Fig. 4d) tends to increase in future scenarios, both in P_A1B (KS = 1) and in E_A1B. In contrast to the case of sea-grid

points, the distributions of ts' over land in PROTHEUS and ECHAM5/MPI-OM are always very similar. The different behaviours of the sea- and land-grid points with respect to the deviations from the baseline seasonal cycle seem to support the tenet that using a high-resolution interactive ocean model on a small area such as the Mediterranean Sea may still improve specific aspects of regional climate modelling. A more thorough understanding of the nature and evolution of the events that produce the discrepancies in the occurrence of cold events, such as those reported in Fig. 4b, is the focus of on-going research.

3.2. Precipitation (pr)

Over the sea, neither the seasonal cycle of precipitation (pr) nor its deviations pr' exhibit significant variations between P_20C and P_A1B or between E_20C and E_A1B (Fig. 5a,b). However, regional downscaling shows pr over sea to be heavier than with the global driver, especially during summer. This is a result of the different physical parameteri-

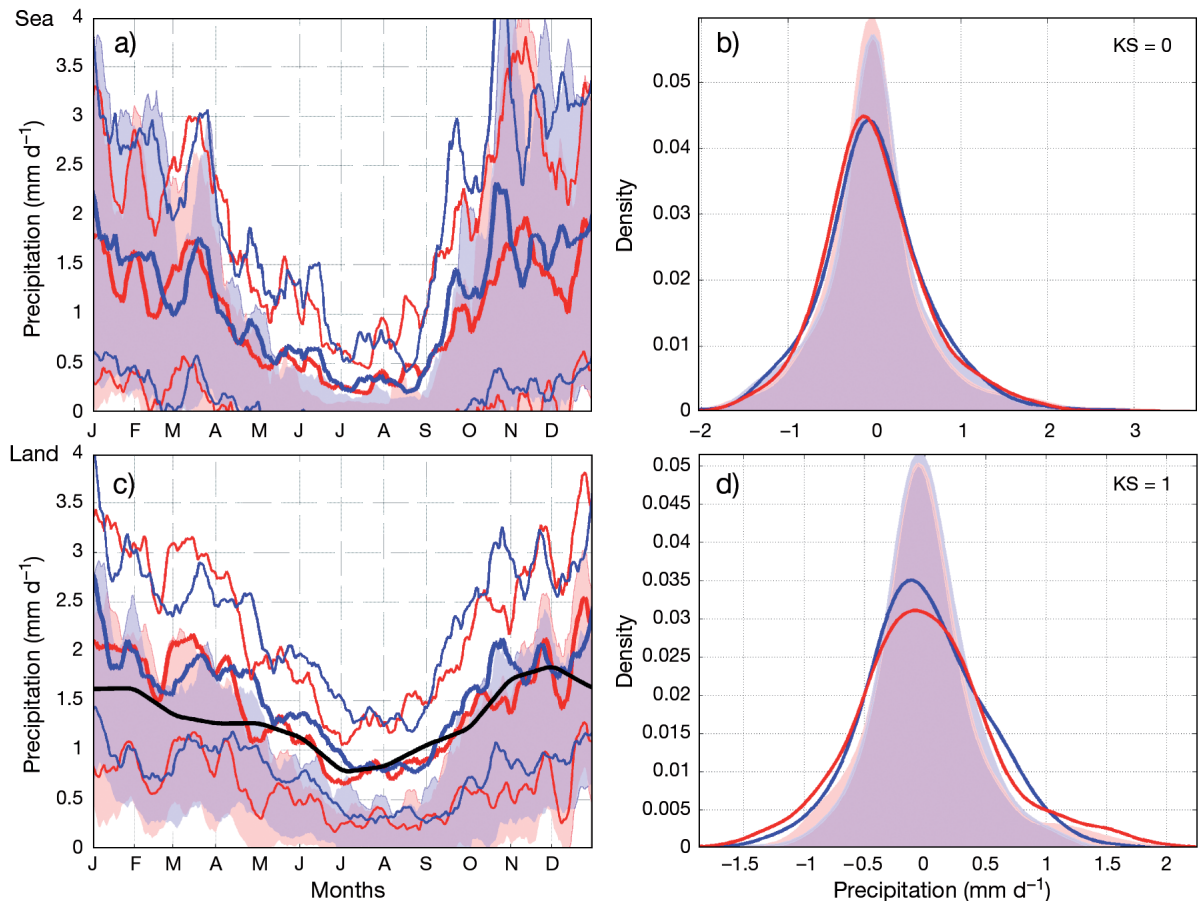


Fig. 5. As in Fig. 4, but for daily rainfall (pr). The black line is the average seasonal cycle of the CRU observational dataset

zation adopted in the 2 models (Zeng et al. 1998, Roeckner et al. 2003), because over the sea we do not expect a direct effect of orography.

On the other hand, the orography, together with the different physical and land parameterization schemes, plays a key role in the representation of pr over land. In Fig. 5c we can observe that the global driver underestimates pr , mainly during the dry season, compared to the climatological seasonal cycle described in the CRU dataset. On the other hand, with PROTHEUS, rainfall is overestimated, as already illustrated in Fig. 2, especially during winter and spring. The average seasonal cycle of pr over land indicates a slight decrease in the scenario P_A1B with respect to the control P_20C during spring and autumn. This variation, however, lies within the range of inter-annual variability (Fig. 5c). Again, the global driver shows a similar behaviour, although the global simulations (E_20C and E_A1B) generally exhibit less precipitation and less variability. Large deviations from the mean seasonal cycle are more frequent in P_20C and P_A1B than in E_20C and E_A1B (lightly shaded red and blue in Fig. 5d). With regional downscaling, the distribution

of deviations shows that intense precipitation events tend to increase also in P_A1B with respect to P_20C. More frequent intense precipitation events over land in a warmer climate are consistent with the greater amounts of specific humidity possible. Larger saturation levels under higher temperatures are neutral to condensation and rainfall over the sea where motion is mostly horizontal (Fig. 5b). On the other hand, due to the presence of topographic uplift, more intense rainfall events over land may be triggered. A more detailed analysis of the nature and frequency of large deviations from the average temperature and rainfall cycles is presented in Section 4.

3.3. Evaporation (et)

Another key variable affecting the hydrological cycle is evaporation (et) (Fig. 6). The average seasonal cycle of evaporation over sea described in the OAFUX dataset exhibits a well-defined minimum in May and a maximum during fall. The P_20C seasonal cycle exhibits similar features (i.e. a minimum in May, a maximum in September followed by a plateau

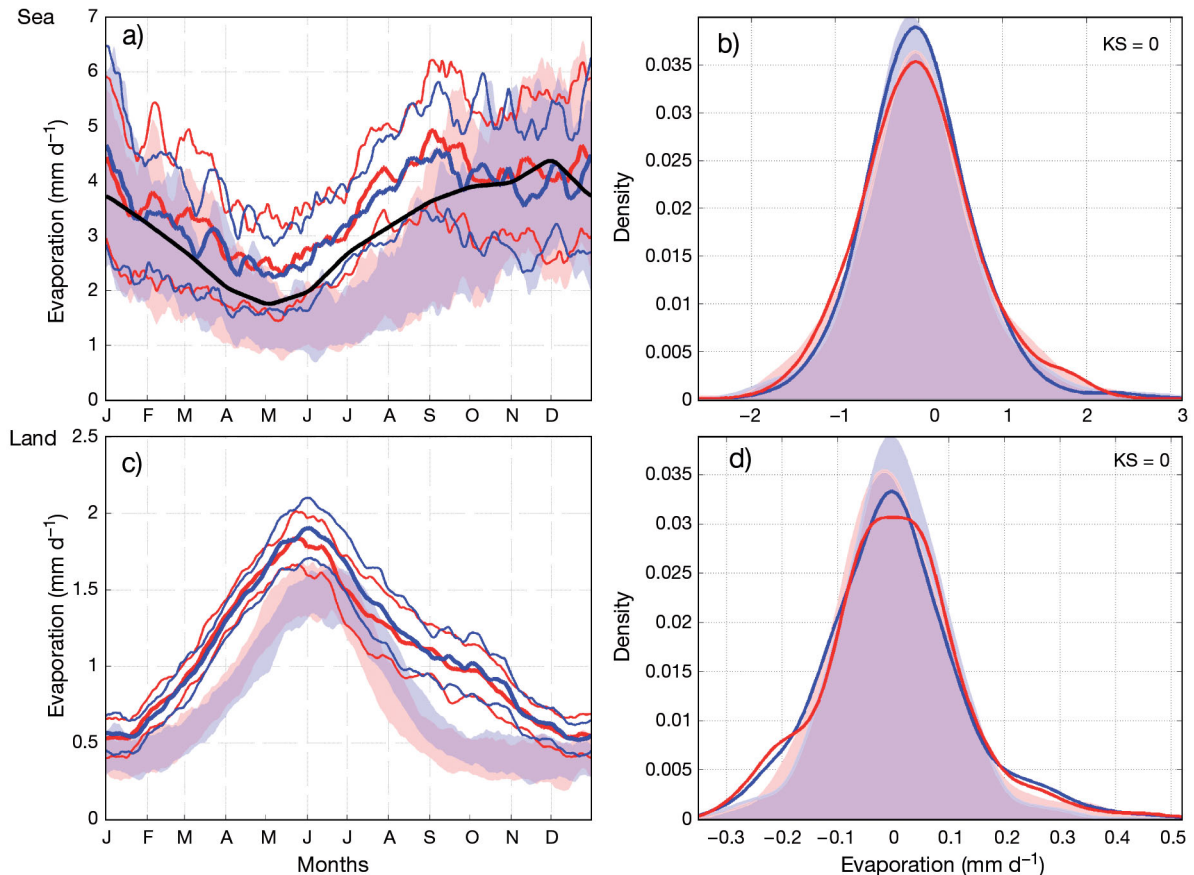


Fig. 6. As in Fig. 4, but for evaporation (et). The black line is the average seasonal cycle of the OAFUX observational dataset

during fall), although with overestimated et values during summer. The average seasonal cycle shown in Fig. 6a suggests that P_A1B patterns closely follow P_20C patterns. In P_A1B only slightly stronger inter-annual variability is noted. In the case of et , the seasonal cycle produced by the global driver (both E_20C and E_A1B simulations) is very different from the case of regional downscaling, especially during summer, when et in the global driver is significantly weaker. The minimum et is delayed to June, and there is no relative maximum in September. This discrepancy in the description of the seasonal cycle of et must be related to the different representations of surface winds and temperatures (Artale et al. 2010), together with the different representations of air–sea fluxes in the 2 models (described in Zeng et al. 1998, Roeckner et al. 2003). Also, in the case of the global driver, no significant variations in E_A1B from E_20C can be detected.

The distribution of deviations from the mean seasonal cycle (Fig. 6b) does not show a significant difference according to the KS test ($KS = 0$), although, in P_A1B, the events of intense et ($\geq 1.5 \text{ mm d}^{-1}$) seem to be slightly more frequent.

Over land, P_A1B shows slightly less evaporation than P_20C during summer, but well within the inter-annual variability; this is probably linked to drying of the soil due to decreased rainfall during spring (Fig. 5c). In the ECHAM5/MPI-OM representation of an average seasonal cycle, a shift in the summer maximum of et occurs. The summer maximum in the global driver is placed on late June at around 1.3 mm d^{-1} , while in PROTHEUS it occurs by the end of May at around 1.7 mm d^{-1} . Generally, during summer, less evaporation is permitted in the global model, which adopts a single-layer surface scheme to describe air–land interactions (Roeckner et al. 2003). The different surface scheme, together with possible differences in land cover, may contribute to these dissimilarities (Alessandri et al. 2007, Anav et al. 2010). However, E_A1B also shows slightly lower et during summer. The distribution of deviations from the mean seasonal cycle does not change in the regional scenario simulation, and it is also quite similar in ECHAM5/MPI-OM (Fig. 6d).

3.4. Water budget (WB)

We consider the freshwater budget of the Mediterranean an important diagnostic indicator that integrates the combined effect of the different components discussed in this section.

By aggregating the total runoff over the catchment basin reported in Fig. 1c, we only consider an approximation of the actual time-dependent river discharge. To obtain a more accurate description of the variability of the river discharge we should account for the appropriate delay between the total runoff at a given point in the catchment basin and the discharge at the river mouth (Hagemann & Jacob 2007). Nevertheless, the total runoff provides useful diagnostics for the overall hydrological cycle in the catchment basin. In order to compare the results of the regional model to those of the global driver, we also apply the same procedure of integration over the interpolated TRIP dataset for the total runoff from the ECHAM5/MPI-OM simulations. In particular, as discussed in Section 2.1, the contribution of the Black Sea to WB in the Mediterranean is derived with PROTHEUS by run-time rescaling of its interior WB (river discharge plus precipitation minus evaporation over Black Sea region). To consistently compare the results from PROTHEUS to the global model, we apply the same linear transfer function to the aggregated runoff of the global driver simulation.

Starting from the components discussed in the previous sections, we can now compute the water budget WB as:

$$WB = et_{\text{sea}} - pr_{\text{sea}} - R - B$$

where R is the total runoff over the whole Mediterranean catchment basin and B is the inflow from the Black Sea.

Good agreement between P_20C and the R value estimated by Struglia et al. (2004) is found for the dry season (May–September), while an overestimation is present in winter and fall (Fig. 7a). This observational estimate is systematically below the values reported by Ludwig et al. (2009) and Sanchez-Gomez et al. (2011). In P_A1B an overall decrease in river runoff can be observed, mainly during spring and summer. The ECHAM5/MPI-OM simulations seriously underestimate the total runoff R , especially during summer. Indeed, as already indicated for pr over land, large deviations from the mean seasonal cycle are more frequent in P20C and in P_A1B than in E_20C and E_A1B (lightly shaded red and blue in Fig. 7b), where the distribution of deviations from the seasonal cycle is very close to a normal distribution. The seasonal cycle of the Black Sea discharge (Fig. 7c) in P_20C is in good agreement with the values estimated by Stanev et al. (2000), especially for winter and fall. During spring and summer, a clear overestimation is reported. Moreover, the summer minimum in the inflow is delayed by around 1 mo in the PROTHEUS simulation, with respect to the seasonal

cycle reported by Stanev and co-authors. On the other hand, the global simulations—both present climate and scenario—are affected by strong underestimation, thereby implying significant improvement by regional downscaling. No relevant differences arise in the P_A1B representation of the seasonal cycle, although Fig. 7d exhibits significant changes in the distribution of deviations from it ($KS = 1$).

As shown in Fig. 8a, inter-annual variability in the total freshwater budget of the regional model follows the global model very closely. The same upward trend is detected in both simulations (Table 1). This is not surprising as the annual WB over a relatively small area such as the Mediterranean is driven by the global scale (Mariotti & Dell'Aquila 2011). However, the regional model shows a lower deficit of water consistent with the higher level of rainfall over land during the entire seasonal cycle, as shown in Fig. 5c. This result is also consistent with Sanchez-Gomez et al. (2009), who report a lower water deficit of re-

gional climate models with respect to global models.

Significant differences between the regional and global climate models also exist in the seasonality of WB (Fig. 8b). The regional climate model anticipates the peak of the dry season with respect to the global driver. This result is consistent with the analysis performed by Sanchez-Gomez et al. (2011) on an ensemble of regional climate models, showing that the strongest drying over a very similar area is usually around August. In particular, a comparison of the seasonal cycles of fundamental components of WB (reported in Figs. 5–7) suggests that the main contribution to an anticipated dry season is best described by et over the sea (Fig. 6). By taking into consideration similar results presented by Sanchez-Gomez et al. (2011), we consider this to be a robust result of high-resolution models with respect to global drivers, given their ability to provide a better description of the local processes affecting et , including wind bursts, temperature and humidity.

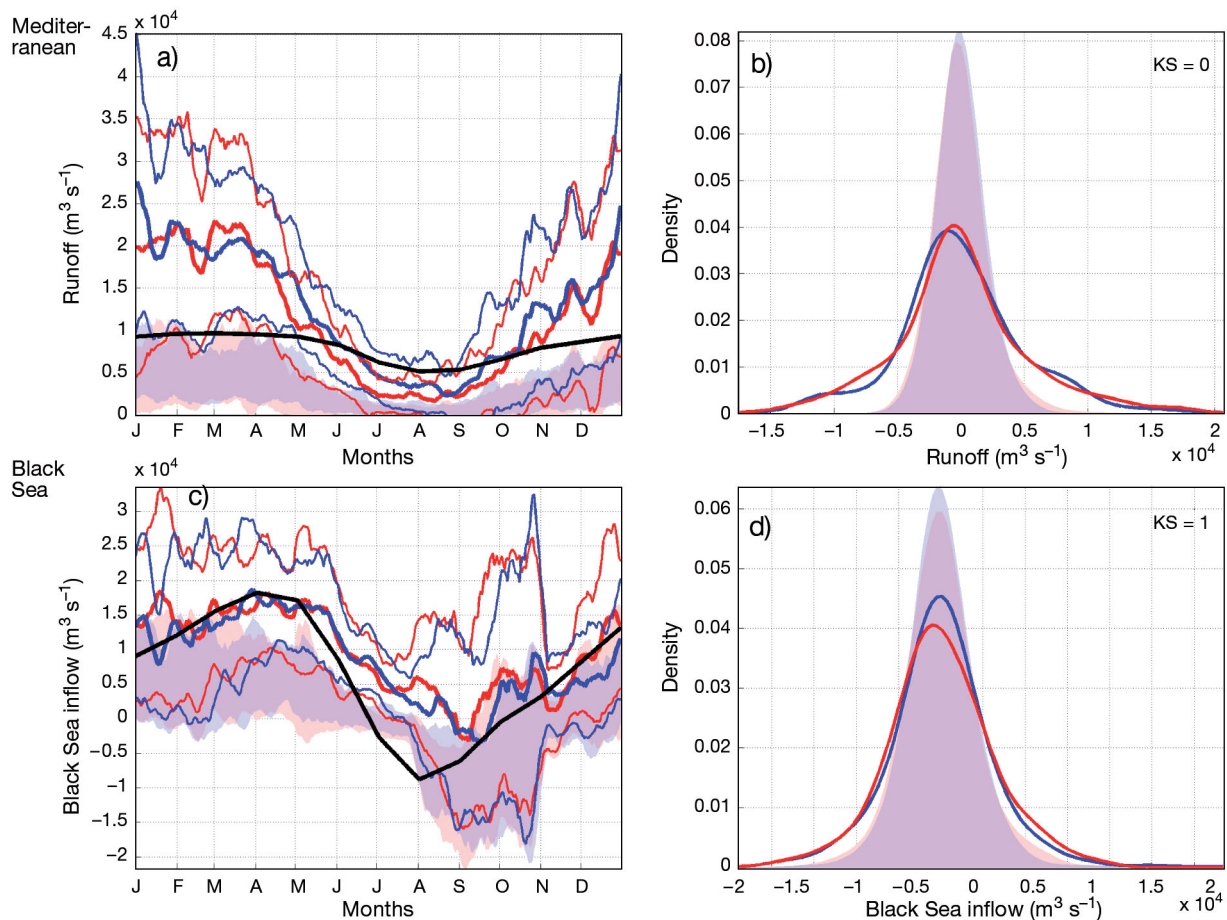


Fig. 7. (a,b) As in Fig. 4, but for the total runoff (surface + drainage) R integrated over the Mediterranean catchment basin (MED; TRIP dataset). The black line in Panel a is the seasonal cycle of the Mediterranean discharge estimated by Mariotti et al. (2002). (c,d) As in Fig. 4, but for the Black Sea inflow B . The black line in Panel c is the seasonal cycle of the Black Sea inflow estimated by Stanev et al. (2000)

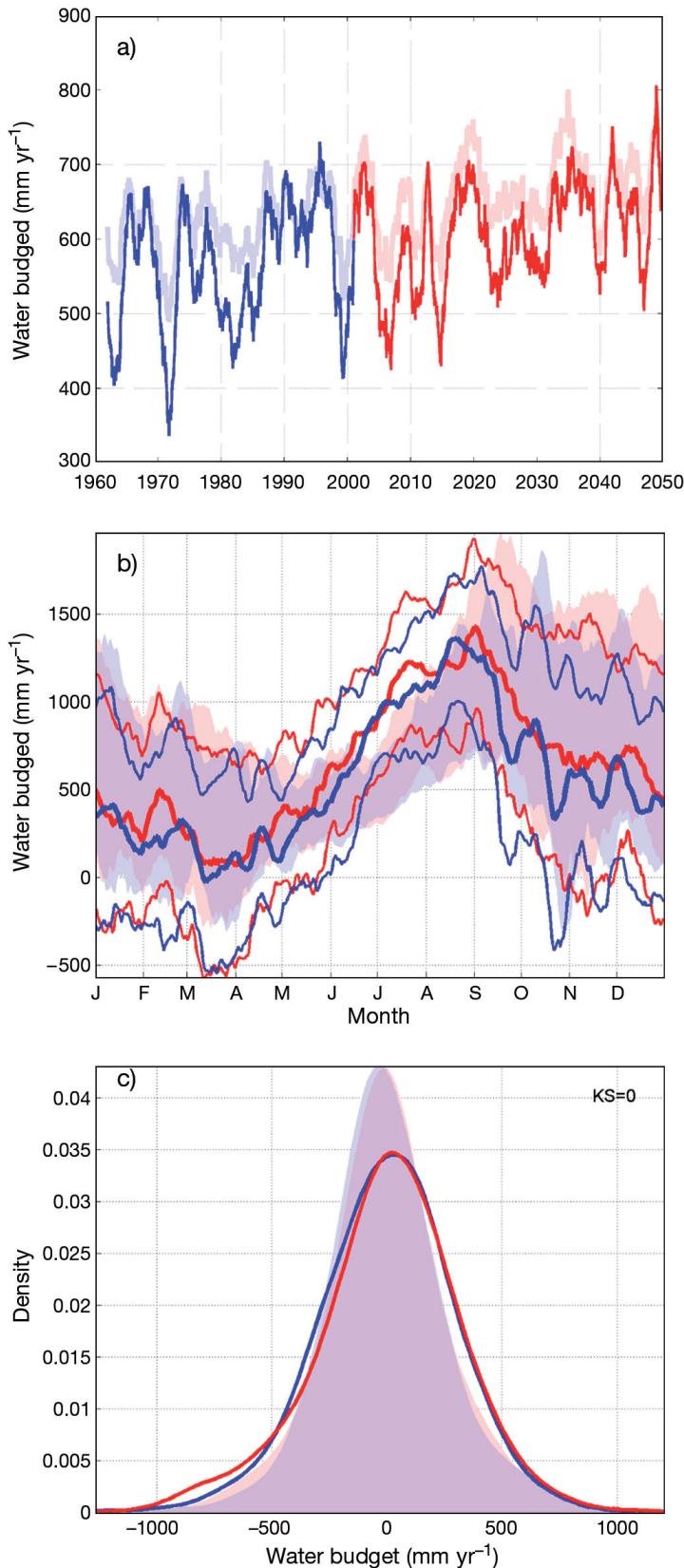


Fig. 8. (a) As in Fig. 2, but for the water budget WB . (b,c) As in Fig. 4a,b, but for the water budget WB

A further interesting comparison with the results presented by Sanchez-Gomez et al. (2011) concerns the amplitude of the inter-annual variability in the seasonal cycle (Fig. 8b), which is comparable with the multi-model ensemble variance. For example, Fig. 8b shows that, during the peak of the dry season in August, the amplitude of the inter-annual variability in the seasonal cycle, as estimated by 1 standard deviation around the mean, is between 800 and 1700 mm yr⁻¹. This interval is similar to the range of values spanned by the ensemble simulations considered by Sanchez-Gomez et al. (2011). Although model ensembles are necessary in order to assess the reliability of model predictions, the comparison of Fig. 8b with Sanchez-Gomez et al. (2011, their Fig. 3) suggests that, for practical purposes, the statistics of climate parameters derived by a multi-year simulation of a single model may already provide a first quantitative insight on the distribution of potential long-term fluctuations.

4. IMPACTS

An important objective of the present study is to understand the advantages that end-users may expect by adopting a high-resolution regional earth system model for the Euro-Mediterranean region in place of the corresponding, coarser, global driver as a primary resource of data for impact-oriented studies. Key impact indicators are the frequency of large temperature and precipitation deviations from the average seasonal cycle, the aridity index, snow cover extension and river discharge. As in Section 3, we compare the 20C period (1961–1970) with the A1B period (2041–2050).

4.1. Large anomalies

Following the analysis of Section 3 on the distribution of aggregated indices of key atmospheric and hydrological variables, we now focus on the tails of those distributions. In particular, we consider the large anomalies of temperature and rainfall over land. We define as *large anomalies* for an atmospheric variable Q those events for which the index Q'_i , representing the deviation from the reference seasonal cycle, exceeds a fixed threshold. By selecting a fixed threshold below or above the corresponding seasonal cycle, we seek to emphasize the occurrence of anomalies regardless of any possible model bias. For example, an increase of 2°C in warm epi-

sodes during summer should be regarded as a potential increase in risk exposure even if the prevailing seasonal cycle of the considered model is biased to be colder than present climate observations (Fig. 4). We arbitrarily set the threshold level to ± 2 standard deviations of the distribution of $Q'_{1961-1970}$ over land in P_20C. Summarizing, the large anomaly events can be defined as follows:

$$\begin{aligned} \text{Positive anomalies} &= Q'_i > 2\sigma(Q')|_{P_{20C}} \\ \text{Negative anomalies} &= Q'_i < 2\sigma(Q')|_{P_{20C}} \end{aligned}$$

With this definition we do not account for the details of the spatial pattern of a specific event: the large anomaly events are selected by considering all land-grid points within the Euro-Mediterranean

domain defined in Section 2. Therefore, we focus on large-scale effects showing that even on the large scale—comparable to that of the domain of the regional simulation—the PROTHEUS system amplifies some of the tendencies in the occurrence of large anomalies produced by the global driver.

Cold events (i.e. $ts' < -2\sigma(ts')|_{P_{20C}} = -1.9\text{ K}$) have a significant impact on a whole range of human activities, from agriculture to the energy sector. In P_20C, cold episodes occur mostly during cold seasons, in winter and autumn (Fig. 9a; blue bars). In P_A1B (Fig. 9a; red bars), the total number of cold events is nearly doubled (from 102 in the present climate to 193 in the scenario). Most importantly, in P_A1B, there is a large increase in the number of cold events

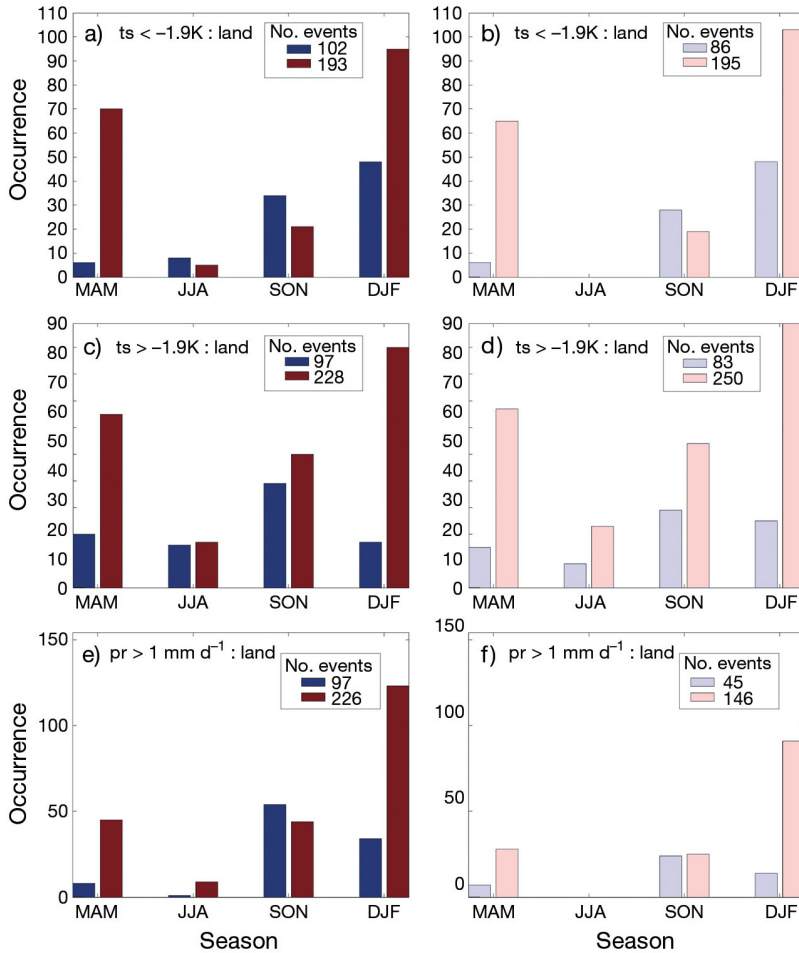


Fig. 9. Number of large anomalies from the seasonal cycle for each season (a,c,e) according to PROTHEUS and (b,d,f) the corresponding global ECHAM5/MPI-OM simulations over the Mediterranean region (land points). Large discrepancies are defined as those with anomaly values exceeding a threshold arbitrarily set at ± 2 standard deviations from the mean reference P_20C seasonal cycle. The blue bars represent the period 1961–1970; the red bars represent the period 2041–2050; the corresponding light colours are for ECHAM5/MPI-OM. MAM: March, April, May; JJA: June, July, August; SON: September, October, November; DJF: December, January, February

during spring and a decrease in cold events during autumn. In other words, P_20C and P_A1B show a different seasonality in the occurrence of cold events. Such a shift in the seasonality of cold events is already present in the global driver (Fig. 9b). However, the effect is amplified in regional downscaling, with the number of cold events in P_A1B considerably exceeding the number of cold events in E_A1B. Increasing probability of cold events during spring increases the probability of frost days during a critical stage of important perennial crops (olives, grapes and other fruits), especially in the Mediterranean area (Ponti et al. 2009 and references therein).

Warm anomalies (i.e. $ts' > 1.9\text{ K}$) are mostly observed during autumn in P_20C and E_20C (Fig. 9c,d; blue bars). In the scenarios (P_A1B and E_A1B), the total number of warm events is more than doubled and the seasonal distribution changes, with most of the events occurring in winter and spring. During spring, the probability of both cold and warm events increases, and downscaling tends to amplify this effect with respect to the global driver. In the case of warm anomalies, the relative seasonal distribution of events is similar in PROTHEUS and ECHAM5/MPI-OM. The combination of fluctuations in the average seasonal cycle and of the deviations from it suggests that, even in a warming scenario, the increasing occurrence of cold events dur-

ing specific periods of the seasonal cycle may be of concern.

For intense rainfall (i.e. $pr' > 1 \text{ mm d}^{-1}$), Fig. 9e shows an increase in days characterized by strong precipitation in P_A1B with respect to P_20C. A closer look at the seasonality of strong precipitation indicates an increase in intense rainfall during winter and spring, with similar tendencies in downscaling and in the global driver. Horizontal resolution plays a central role in the description of intense rainfall events. A coarser model aggregates the water available for precipitation over larger cells, thereby decreasing the overall frequency of intense events, and a steep orography in the regional models facilitates the triggering of more intense rainfall in a warmer and moister environment. As a consequence, the total number of intense episodes is always considerably larger in the case of high-resolution downscaling (Rebora et al. 2006) and the increase, in the modelled future scenario, of the number of intense episodes is also amplified.

To characterize the patterns of intense precipitation in the different scenarios considered, we report the spatial distribution of rainfall anomalies for the seasons during which the largest number of intense events occurs (Fig. 10). The strongest anomaly of pre-

cipitation in P_20C occurs during autumn over the Iberian Peninsula, over the Balkan chain and over the Tyrrhenian coast of southern Italy (Fig. 10a). In contrast, in P_A1B, the largest deviations from the seasonal cycle occur during winter over the Alps, in northern Italy and over a large part of the Iberian Peninsula (Fig. 10c). In E_20C and E_A1B, the area of intense rainfall upwind of major orographic systems (e.g. over Italy and the Balkans) is missing due to the coarse representation of orography. As a consequence, in ECHAM5/MPI-OM, westward synoptic perturbations carry more humidity and produce larger amounts of rainfall over Turkey than is the case in regional downscaling. The occurrence of intense rainfall events over the Iberian Peninsula is also amplified in the regional downscaling.

4.2. Aridity index (AI)

The aridity index (AI; UNEP 1992) is defined by the ratio:

$$AI = \frac{pr}{PET} \quad (3)$$

where pr is the annual cumulated precipitation and PET is the annual potential evapotranspiration. AI

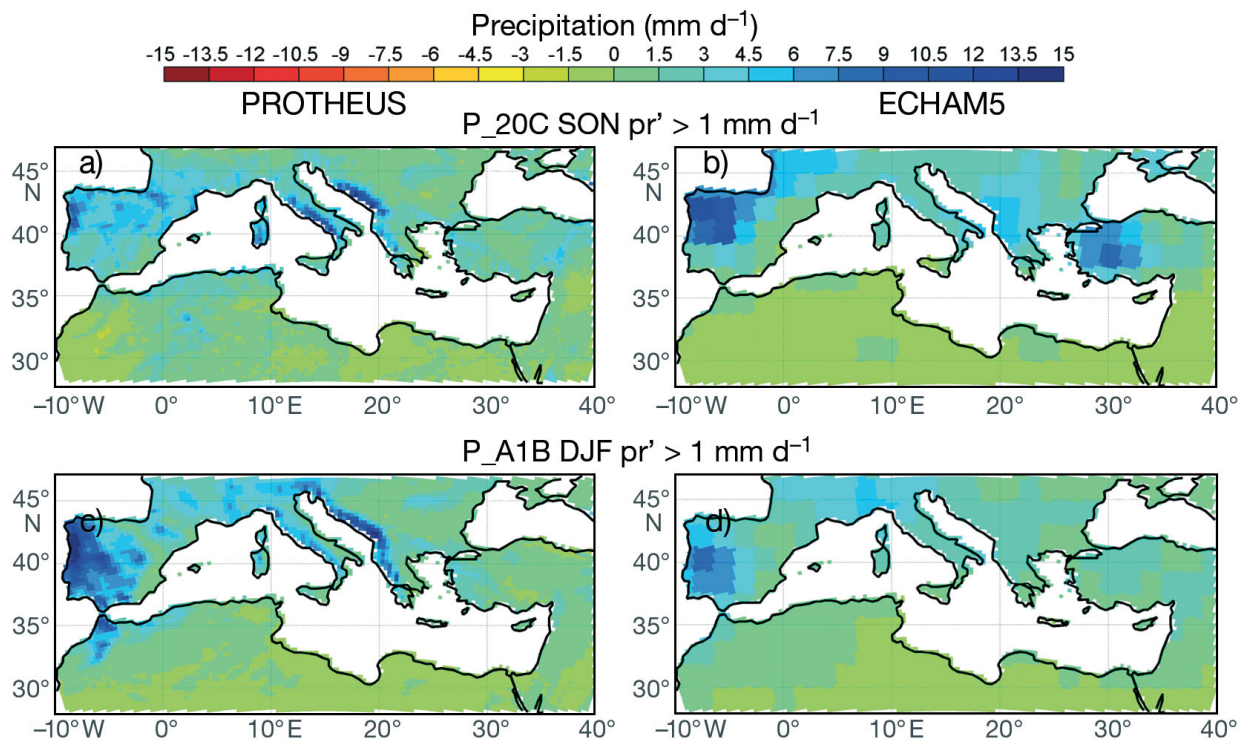


Fig. 10. Anomaly composites of large positive deviations in rainfall according to (a,c) PROTHEUS and (b,d) ECHAM5/MPI-OM simulations for 20C (SON anomalies) and for A1B (DJF anomalies) (see Fig. 9e,f). We show the composites only for the seasons during which the largest number of intense rainfall events occurs (see Fig. 9). The global driver patterns are reported on the PROTHEUS grid to make comparison easier

can be used to quantify precipitation availability over atmospheric water demand (i.e. water input or gain against the potential output or loss) and is widely used as a measure of arid/humid regimes, also for the Euro-Mediterranean region (e.g. Safriel 2009). Moreover, it can help in quantifying agricultural production, especially for rain-fed crops. Different definitions of *PET* can be adopted, which would result in different definitions of the *AI* (Gao & Giorgi 2008). We use the Penman definition of *PET* (Allen et al. 1998):

$$PET = 0.408 \frac{\Delta(R_N) + 900\gamma \frac{u_2}{T_2}(e_s - e_a)}{\Delta + \gamma(1 + 0.34u_2)} \quad (4)$$

where Δ is the slope of the Clausius-Clapeyron equation, $R_N = R_{SW} - R_{LW}$ is the difference between the incoming solar shortwave radiation R_{SW} and the outgoing long-wave radiation R_{LW} , e_s is the anemometric (measured at a nominal height of 2 m) saturation vapour pressure, e_a is the vapour pressure, γ is the psychrometric coefficient which depends on the atmospheric pressure, u_2 is the wind speed measured at 2 m height and T_2 is the temperature measured at 2 m height expressed in K. With a minor loss in accuracy, we consider a reference psychrometric coefficient γ at height h above sea level for a standard atmosphere at 20°C with sea level pressure of 1013 mb, such that:

$$\gamma = 0.665 \times 10^{-3} \left[101.3 \left(\frac{293 - 0.0065h}{293} \right)^{5.26} \right]$$

We adopted Eq. (4) for processing both PROTHEUS and global data in order to derive the *AI*. A critical threshold for this index is $AI = 1$, below which annual evapotranspiration exceeds the cumulated rainfall and plants are likely to suffer under the lack of water.

Fig. 11a,b shows mean values for *AI* in P_20C and E_20C, respectively. The solid black line marks the contour corresponding to $AI = 1$, hence distinguishing the arid from the humid zones. In P_20C, many areas along the Mediterranean coasts (South Spain up to the Pyrenees, North Africa, Sicily, Sardinia, the Adriatic coasts of Italy, part of Greece) are characterized by $AI < 1$, as well as large regions of south-eastern Europe. This P_20C spatial distribution closely follows the maps of arid zones in the Euro-Mediterranean region that have already been designated in several observational studies (UNEP 1992, Safriel 2009). In areas characterized by a steep orography, such as the Balkans and Italy, the regional downscaling distinguishes patterns of humid/dry sub-regions that cannot be captured by the global

driver, which uniformly classifies such regions as humid (Fig. 11b). Large discrepancies between P_20C and E_20C exist over Anatolia and west of the Black Sea. Such differences are coherent with the patterns of intense rainfall shown in Fig. 10, thereby confirming that ECHAM5/MPI-OM overestimates rainfall over these semi-arid regions.

By looking at a composite index such as *AI*, accounting for both evaporation and precipitation, the differences between downscaling and the global driver are easily amplified. For example, the *AI* trends show different behaviours in P_A1B and E_A1B. In the differences between P_20C and P_A1B (Fig. 11c) we detect a spatial pattern in the fluctuations of *AI* linked to the orography that surrounds the Mediterranean, e.g. a negative trend in the *AI* over the northern Iberian Peninsula, over the Pyrenees, south of the Alps and around the Aegean Sea. The corresponding pattern obtained from the difference between E_20C and E_A1B is very noisy (Fig. 11d).

4.3. Snow cover

Snow cover extension is an important indicator as it affects a wide range of human activities, especially in densely populated environments such as the Euro-Mediterranean area (tourism, water storage, energy production). In mountain regions, the snow cover duration and distribution can largely affect the length of the growing season, with direct impacts on local ecosystems (Jacobson et al. 2004). Also, in a Mediterranean climate characterized by abundant rain during winter and hot/dry summers, glacier dynamics are the result of a balance between the accumulation of snow during winter and summer melting, such that even under a warming scenario glaciers can undergo periods of expansion (Calmanti et al. 2007). The regional climate model adopted in the present study, which improves the description of steep orography and SST compared to the global driver, refines the quality of information on the trends in snow cover and on the related impacts.

We report in Fig. 12 the seasonal 20C averages together with the A1B-20C snow cover trends for DJF and MAM. For comparison, we also report the satellite-based climatological snow cover extension of the EASE dataset provided by Armstrong & Brodzik (2005) (Fig. 12e,f). In agreement with the satellite estimate, the snow cover extension in the simulation P_20C follows the orography during the winter (Fig. 12a), when the Alps, the Pyrenees and the

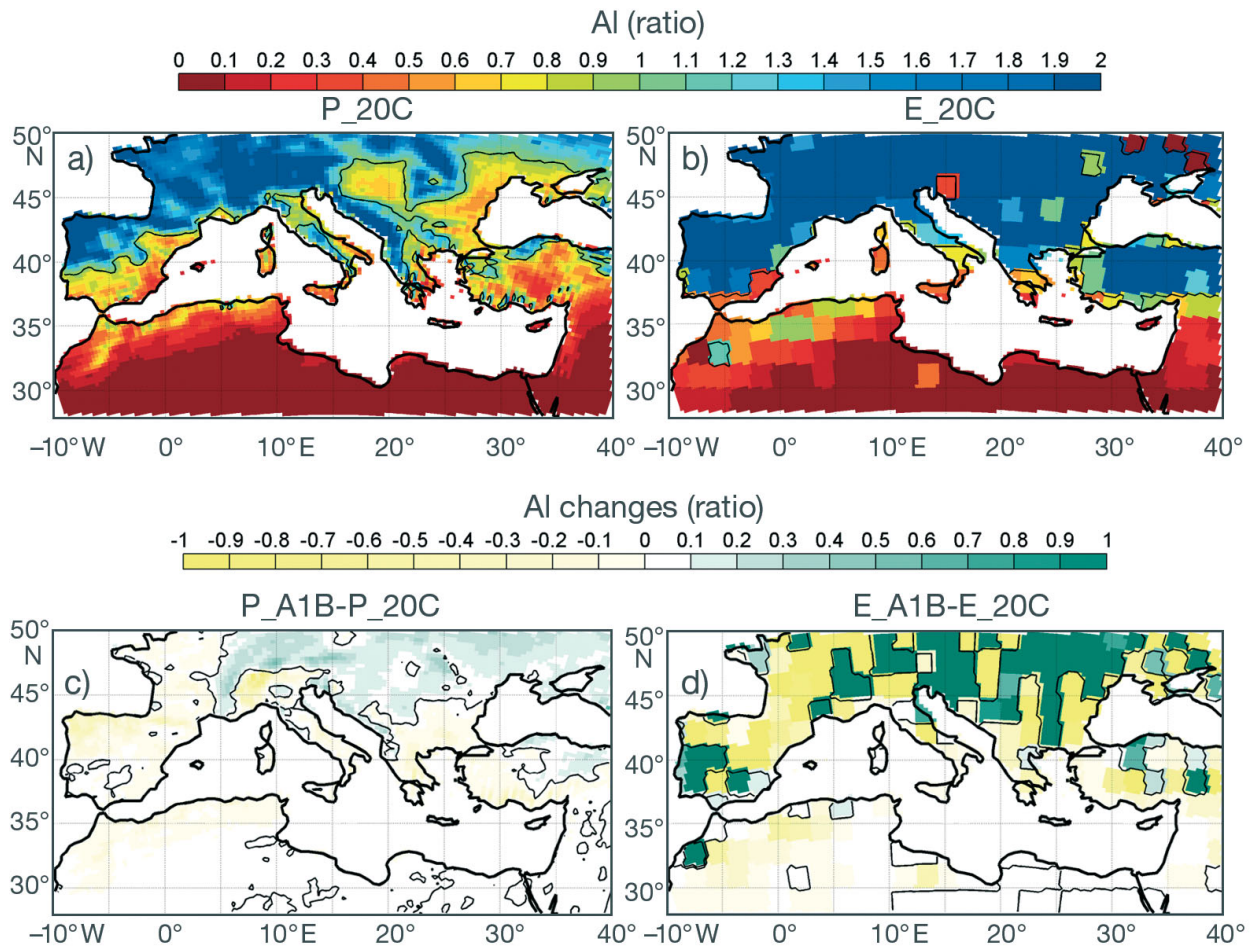


Fig. 11. Aridity index (*AI*) according to PROTHEUS and ECHAM5/MPI-OM simulations. (a,b) Mean values in P_20C and E_20C, respectively. Solid lines: $AI = 1$. The reference period is 1961–1970. (c,d) *AI* changes (A1B-20C). Solid lines: zero difference contours. The global driver patterns are reported on the PROTHEUS grid

Carpathian and Anatolian mountains are covered by a consistent snow layer. On the other hand, P_20C underestimates the snow cover over the eastern European lowlands (Danube Basin). During spring the snow layer over the higher mountains persists (Fig. 12c). In E_20C, a wide extension of snow cover is depicted for DJF (with an overestimation over Anatolia), whereas spring snow cover is underestimated (Fig. 12d). In P_A1B, a negative trend in snow cover characterizes PROTHEUS over the Alps and to a minor degree over the Pyrenees, Carpathian and Pontus mountains east of Turkey. The snow cover over the Alps significantly decreases due to the combined effect of an overall increase in temperature (Fig. 4) and a locally enhanced water deficit (Fig. 11c). A decrease in Alpine snow cover can critically affect the seasonality of the hydrological cycle in the Mediterranean basin, as mountain glaciers are an important source of water for most river systems in

this area. In E_A1B, a negative trend in snow cover is observed north of the Alps, over eastern Europe, and over eastern Turkey during winter, and an increase in snow cover over the northern Adriatic Croatian coast (Fig. 12i). Moreover, during MAM (Fig. 12l), E_A1B shows increasing snow cover north of the Alps and in eastern Europe, thereby providing a completely different picture of the impact of future climate fluctuations on snow cover with respect to regional downscaling.

4.4. Po River discharge (*mrro*)

River discharge is the outcome of a range of processes described by climate models, from air–soil interaction to condensation and atmospheric convection, with a relevant role by orography and snow melting. We focus our analysis on the Po River water

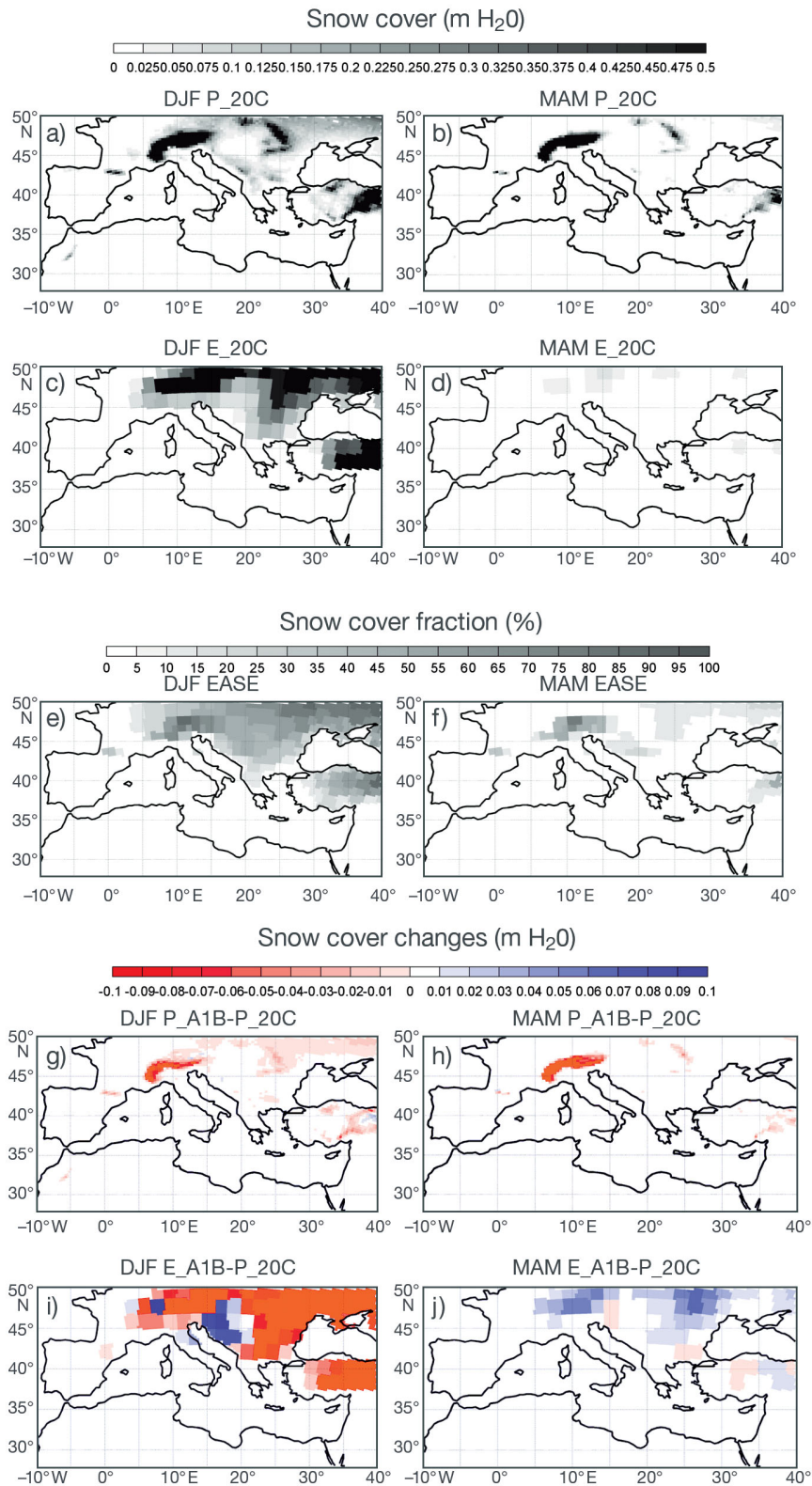


Fig. 12. Snow cover. (a,c,e) Seasonal DJF 20C average in PROTHEUS, ECHAM5/MPI-OM simulations and in the climatological EASE dataset, respectively. Units are m H₂O for PROTHEUS and ECHAM5/MPIOM, while percentage fraction is used for EASE. (b,d,f) As in Panels a, c and e, but for MAM. (g,h) DJF and MAM seasonal changes (A1B minus 20C) in PROTHEUS and (i,j) ECHAM5/MPI-OM simulations. The global driver patterns are reported on the PROTHEUS grid

source, which is mainly in the Alps. Given the large differences between the global driver and the regional model in the description of orography (Fig. 1) and the significant discrepancies in the effects of snow cover extension (Fig. 12), the Po River is an optimal case to test the improvements in impact studies arrived at through the downscaling of global climate models. Moreover, Po discharge plays a key role in water circulation in the North Adriatic Sea (Artegiani et al. 1997).

In Fig. 13, the average seasonal cycle of *mrr* is compared to the discharge observed at the Pontelagoscuro station (close to the Po delta) from the RivDIS dataset (Vörösmarty et al. 1998). In P_20C and P_A1B, the mean level of total runoff ($1460 \text{ m}^3 \text{ s}^{-1}$ in P_20C; $1402 \text{ m}^3 \text{ s}^{-1}$ in P_A1B) is consistent with an observed average river discharge of about $1500 \text{ m}^3 \text{ s}^{-1}$, whereas, in the global model, the aggregated total runoff of the Po River is consistently lower ($520 \text{ m}^3 \text{ s}^{-1}$ in E_20C; $517 \text{ m}^3 \text{ s}^{-1}$ in E_A1B). The seasonal cycle of the Po discharge also shows significant differences in the comparison between the global driver and regional downscaling. In the case of P_20C, a plateau of large total runoff is maintained

throughout April and May, and the minimum is reached in August–September. A relative maximum is also present during fall, while during November–December we note decreasing Po discharge, related to snow precipitation in the Alps. These features are in agreement with the observations. In E_20C, the total runoff peaks in April and starts to decrease until it reaches its minimum by the end of June. The scenarios P_A1B and E_A1B shift the phase of maximum runoff slightly forward. In particular, in P_A1B, the decreasing phase of summer river discharge is steeper than in P_20C, leading to a minimum already in July. All the differences between present climate and future scenarios are within the range of inter-annual variability, both for the global driver and for regional downscaling. However, regional downscaling appears to amplify the differences between present climate and future scenarios that are already suggested by the global driver, with a larger difference in total runoff of the Po River, especially during summer.

The distribution of deviations from the seasonal cycle is very close to normal in the case of the global driver (Fig. 13b). In contrast, in regional downscal-

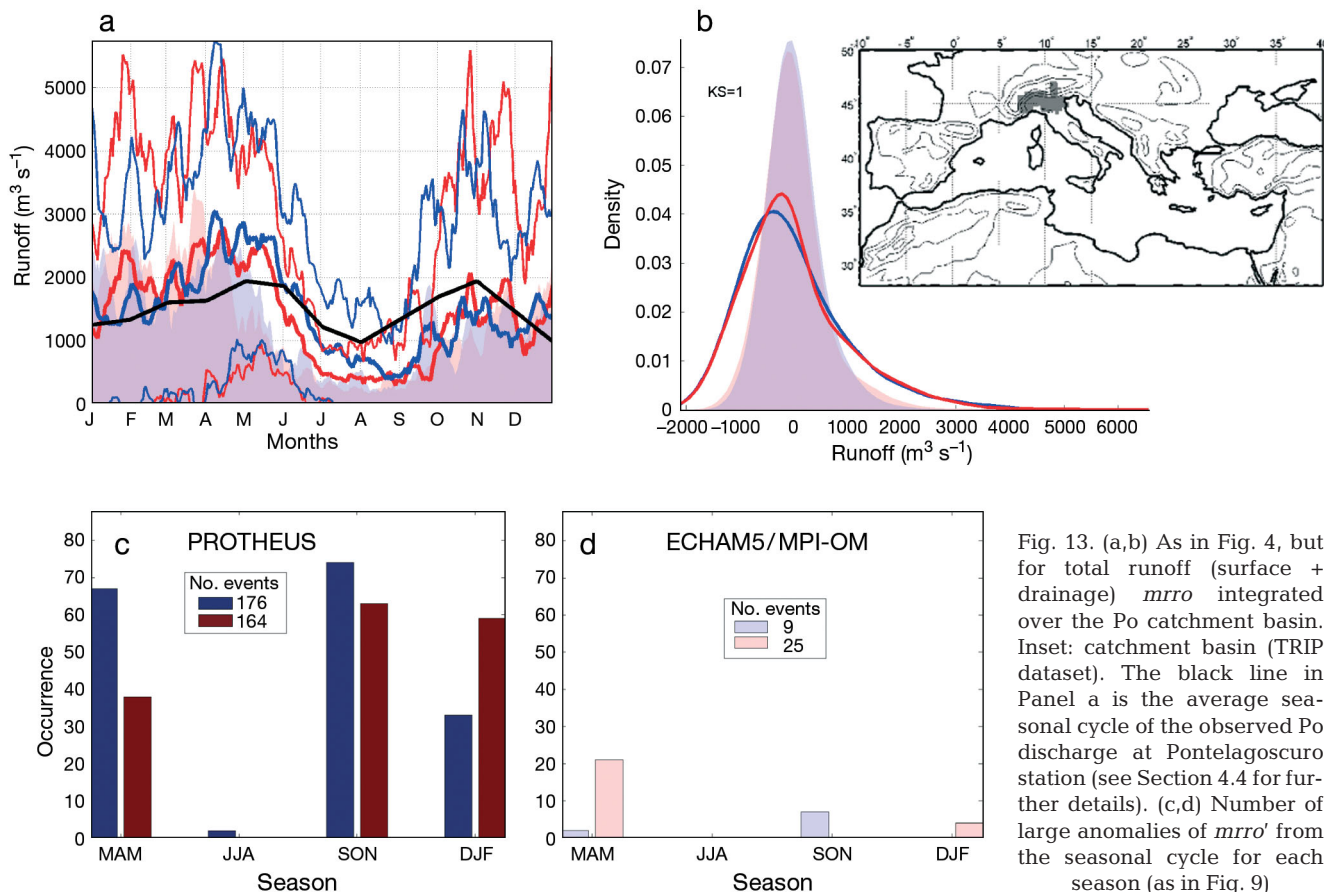


Fig. 13. (a,b) As in Fig. 4, but for total runoff (surface + drainage) *mrr* integrated over the Po catchment basin. Inset: catchment basin (TRIP dataset). The black line in Panel a is the average seasonal cycle of the observed Po discharge at Pontelagoscuro station (see Section 4.4 for further details). (c,d) Number of large anomalies of *mrr'* from the seasonal cycle for each season (as in Fig. 9)

ing, the distribution has a significantly positive skew, suggesting improved capture of the distribution of flooding, which is frequent and has a severe societal impact. The probability of dry events is also larger using regional downscaling, both for the present climate and for the future scenario. Overall, regional downscaling shows larger mean runoff and greater variability, which are, at least qualitatively, closer to observations.

Fig. 13b shows a slight shift in the most likely deviations from the seasonal cycle towards zero in the case of P_A1B with respect to P_20C. The shift is statistically significant according to a K-S test at the 99% confidence level and is consistent with the overall lower runoff of P_A1B during summer, leaving less room for negative anomalies in an already drier background with respect to P_20C.

As for the seasonality of large positive deviations, Fig. 13c shows that the number of events decreases in P_A1B during spring and increases during winter with respect to P_20C. These discrepancies are consistent with the evolution of snow cover described in Section 4.3, whereby less snow implies less intense Po runoff during the melting season. By also considering the results presented in Fig. 5c (no significant differences in the seasonal cycle of rainfall between P_20C and P_A1B) and an increase in the number of events of intense rainfall during winter (Fig. 9e), Fig. 13c supports the hypothesis that more intense precipitation in the form of rainfall during winter may increase the possibility of large river runoff during this season. In particular, the number of events with large runoff in P_A1B during winter approaches the number of events produced during fall, the season during which most of the flooding in the Po Valley is currently observed. In comparison, the number of events that exceed the selected threshold in the global model are vanishing (Fig. 13d), and the changes during spring are of the opposite sign with respect to those with downscaling, in agreement with a trend of heavy rainfall (Fig. 9f). In fact, due to the poor representation of orography and the consequent weak signal of the evolution of snow cover over the Alps (Fig. 12), the snow melt during spring in ECHAM5/MPIOM has a negligible role in modulating the Po River discharge.

5. CONCLUSIONS

We use an ocean–atmosphere regional earth system model to study the long-term fluctuations in the prevailing seasonal cycle in an A1B scenario of

future greenhouse gas emissions. The atmospheric component of the regional model is driven by a simulation global scenario performed with ECHAM5/MPI-OM, whereas the oceanic component has an Atlantic box that is forced with anomalies to the Levitus climatology derived from the same global model. The fundamental improvements obtained with this modelling strategy are a partial reduction of the SST bias produced in the driving global simulation and a better representation of the corresponding patterns.

We have adopted a simple scheme of data analysis, with a special focus on large deviations from the average seasonal cycle. This highlights the advantages of adopting a regional high-resolution earth system model as a source of primary data in place of the coarser global driver. We have considered the average seasonal cycle of key atmospheric variables and the probability distribution of the deviations from it. Particular attention has been devoted to the representation of the hydrological cycle and to a few related key indicators of the impact of climate fluctuations on water resources, such as river discharge, the aridity index and snow cover extension.

We consider the present climate and future scenario simulations performed with the PROTHEUS system (Artale et al. 2010), driven by the global model ECHAM5/MPI-OM.

The downscaling performed with the ocean–atmosphere RCM tends to amplify the fluctuations in the SST seasonal cycle already present in the global driver, and to increase the frequency of large temperature anomalies (both warm and cold events). In particular, the differences between the global driver and regional downscaling are larger for sea-grid points, thereby supporting the tenet that even in a small area such as the Mediterranean Sea, using a high-resolution interactive sea improves regional climate modelling.

The different representation of surface temperature affects air–sea fluxes and thereby the seasonality of the moisture availability in the atmosphere. Significant differences in the occurrence and pattern of intense rainfall episodes exist between downscaling and the global driver. In particular, a more accurate description of complex orography surrounding the Mediterranean Sea, as well as of land surface processes, produces more organized patterns in the trends of key impact indicators, such as *AI* and snow cover. On the other hand, the global driver considered in the present study produces extremely noisy results that would prove difficult to interpret in the context of impact studies. Regional downscaling thus

provides a more detailed and reliable description of river runoff in medium/small size river catchment basins than would be captured in a global model. A test case is the Po River (a relatively small catchment basin), for which the PROTHEUS system shows significant skill in describing the baseline seasonal cycle and an internally coherent evolution of future scenarios.

Model ensembles provide an improved basis for probabilistic projections compared to single model realizations (Lambert & Boer 2001, Palmer et al. 2004, Hagedorn et al. 2005). In particular, Hagemann & Jacob (2007) indicate that RCM ensembles can compensate for problems that a driving GCM might have with local-scale processes or parameterizations.

Acknowledgements. The authors thank the Abdus Salam ICTP-ESP group who kindly provided the ECHAM5/MPI-OM boundary conditions for our simulations, performed in the framework of the activities of RL2 of CIRCE-EU projects (EU Project No. 036961). We thank E. Stanev for providing the river runoff dataset. This work is partially funded by the Italian Ministry of Economic Development, Project 2.1.5 'Studi e valutazioni sul potenziale energetico delle correnti marine', framework program MiSE-ENEA.

LITERATURE CITED

- Alessandri A, Gualdi S, Polcher J, Navarra A (2007) Effects of land surface and vegetation on the boreal summer surface climate of a GCM. *J Clim* 20:255–278
- Allen RG, Pereira LS, Raes D, Smith M (1998) Crop evapotranspiration: guidelines for computing crop requirements. Irrigation Drainage Pap No. 56, FAO, Rome
- Anav A, Ruti P, Valentini R, Artale V (2010) 2009: modelling the effects of land-cover changes on surface climate in the Mediterranean region. *Clim Res* 41:91–104
- Armstrong RL, Brodzik MJ (2005) Northern Hemisphere EASE-grid weekly snow cover and sea ice extent, Version 3 (updated 2007). National Snow and Ice Data Center, Boulder, CO (digital media)
- Artale V, Calmanti S, Carillo A, Dell'Aquila A and others (2010) An atmosphere–ocean regional climate model for the Mediterranean area: assessment of a present climate simulation. *Clim Dyn* 35:721–740
- Artegiani A, Paschini E, Russo A, Bregant D, Raicich F, Pinardi N (1997) The Adriatic Sea general circulation. 1. Air–sea interactions and water mass structure. *J Phys Oceanogr* 27:1492–1514
- Bengtsson L, Hodges KI, Roeckner E (2006) Storm tracks and climate change. *J Clim* 19:3518–3543
- Calmanti S, Motta L, Turco M, Provenzale A (2007) Impact of climate variability on Alpine glaciers in northwestern Italy. *Int J Climatol* 27:2041–2053
- Déqué M, Jones RG, Wild M, Giorgi F and others (2005) Global high resolution versus Limited Area Model climate change projections over Europe: quantifying confidence level from PRUDENCE results. *Clim Dyn* 25:653–670
- Elguindi N, Somot S, Déqué M, Ludwig W (2009) Climate change evolution of the hydrological balance of the Mediterranean, Black and Caspian Seas: impact of climate model resolution. *Clim Dyn* 36:205–228
- Gao X, Giorgi F (2008) Increased aridity in the Mediterranean region under greenhouse gas forcing estimated from high resolution simulations with a regional climate model. *Global Planet Change* 62:195–209
- Giorgi F, Lionello P (2008) Climate change projections for the Mediterranean region. *Global Planet Change* 63:90–104
- Giorgi F, Mearns LO (1999) Introduction to special section: regional climate modeling revisited. *J Geophys Res* 104: 6335–6352
- Giorgi F, Bates G, Nieman S (1993a) The multi-year surface climatology of a regional atmospheric model over the western United States. *J Clim* 6:75–95
- Giorgi F, Marinucci M, Bates G (1993b) Development of a second generation regional climate model (RegCM2). I. Boundary layer and radiative transfer processes. *Mon Weather Rev* 121:2794–2813
- Giorgi F, Bi X, Pal JS (2004) Mean, interannual variability and trends in a regional climate change experiment over Europe. I. Present day climate (1961–1990). *Clim Dyn* 22: 733–756
- Hagedorn R, Doblas-Reyes FJ, Palmer TN (2005) The rationale behind the success of multi-model ensembles in seasonal forecasting. I. Basic concept. *Tellus* 57A:219–233
- Hagemann S, Dümenil Gates L (2001) Validation of the hydrological cycle of ECMWF and NCEP reanalyses using the MPI hydrological discharge model. *J Geophys Res* 106:1503–1510
- Hagemann S, Jacob D (2007) Gradient in the climate change signal of European discharge predicted by a multi-model ensemble. *Clim Change* 81(Suppl 1):309–327 (PRUDENCE special issue)
- Jacobson AR, Provenzale A, von Hardenberg A, Bassano B, Festa-Bianchet M (2004) Climate forcing and density dependence in a mountain ungulate population. *Ecology* 85:1598–1610. doi:10.1890/02-0753
- Jungclaus JH, Botzet M, Haak H, Keenlyside N and others (2006) Ocean circulation and tropical variability in the coupled model ECHAM5/MPI-OM. *J Clim* 19:3952–3972
- Lambert SJ, Boer GJ (2001) CMIP1 evaluation and intercomparison of coupled climate models. *Clim Dyn* 17:83–106
- Lucarini V, Calmanti S, Dell'Aquila A, Ruti PM, Speranza A (2007) Intercomparison of the northern hemisphere winter mid-latitude atmospheric variability of the IPCC models. *Clim Dyn* 28:829–848
- Ludwig W, Dumont E, Meybeck M, Heussner S (2009) River discharges of water and nutrients to the Mediterranean and Black Sea: major drivers for ecosystem changes during past and future decades? *Prog Oceanogr* 80:199–217
- Mariotti A, Dell'Aquila A (2011) Decadal climate variability in the Mediterranean region: roles of large-scale forcings and regional processes. *Clim Dyn* 38:1129–1145
- Mariotti A, Zeng N, Jin-Ho Yoon, Artale V, Navarra A, Alpert P, Li LZ (2008) Mediterranean water cycle changes: transition to drier 21st century conditions in observations and CMIP3 simulations. *Environ Res Lett* 3: 044001. doi:10.1088/1748-9326/3/4/044001
- Mariotti A, Struglia MV, Zeng N, Lau KM (2002) The hydrological cycle in the Mediterranean region and implications for the water budget of the Mediterranean Sea. *J Clim* 15:1674–1690
- Marsland G, Haak H, Jungclaus J, Latif M, Röske F (2003) The Max Planck Institute global/sea-ice model with orthogonal curvilinear coordinates. *Ocean Model* 5:91–127
- MEDAR Group (2002) MEDATLAS/2002 database. Mediterranean and Black Sea database of temperature salinity and bio-chemical parameters. Climatological Atlas, IFREMER

- Millot C (1999) Circulation in the western Mediterranean Sea. *J Mar Syst* 20:423–442
- New M, Lister D, Hulme M, Makin I (2002) A high-resolution data set of surface climate over global land areas. *Clim Res* 21:1–25
- Oki T, Sud YC (1998) Design of total runoff integrating pathways (TRIP)—a global river channel network. *Earth Interact* 2:1–37
- Pal JS, Giorgi F, Bi X, Elguindi N and others (2007) Regional climate modeling for the developing world: the ICTP RegCM3 and RegCNET. *Bull Am Meteorol Soc* 88:1395–1409
- Palmer TN, Doblas-Reyes FJ, Hagedorn R (2004) Development of a European multimodel ensemble system for seasonal-to-interannual prediction (DEMETER). *Bull Am Meteorol Soc* 85:853–872
- Ponti L, Cossu QA, Gutierrez AP (2009) Climate warming effects on the *Olea europaea*–*Bactrocera oleae* system in Mediterranean islands: Sardinia as an example. *Glob Change Biol* 15:2874–2884
- Rayner NA, Parker DE, Horton EB, Folland CK and others (2006) UKMO—GISST/MOHSST6—Global ice coverage and SST (1856–2006). UK Meteorological Office. Available from: <http://badc.nerc.ac.uk/data/gisst/>
- Rebora N, Ferraris L, von Hardenberg J, Provenzale A (2006) RainFARM: rainfall downscaling by a filtered autoregressive model. *J Hydrometeorol* 7:724–738
- Roeckner E, Baum G, Bonaventura L, Brokopf R and others (2003) The atmospheric general circulation model ECHAM5. I. Model description. Rep 349, Max Planck Institute for Meteorology, Hamburg
- Roether W, Manca BB, Klein B, Bregant D and others (1996) Recent changes in eastern Mediterranean deep waters. *Science* 271:333–335
- Ruti PM, Dell'Aquila A (2010) The twentieth century African easterly waves in reanalysis systems and IPCC simulations, from intra-seasonal to inter-annual variability. *Clim Dyn* 35:1099–1117
- Safriel U (2009) Status of desertification in the Mediterranean region. In: Rubio JL, Safriel U, Daussa R, Blum WEH, Pedrazzini F (eds) *Water scarcity, land degradation and desertification in the Mediterranean region*. NATO Science for Peace and Security Series, Part I. NATO, Valencia, p 33–73
- Sanchez-Gomez E, Somot S, Mariotti A (2009) Future changes in the Mediterranean water budget projected by an ensemble of regional climate models. *Geophys Res Lett* 36:L21401. doi:10.1029/2009GL040120
- Sanchez-Gomez E, Somot S, Josey S, Dubois C, Elguindi N, Déqué M (2011) Evaluation of Mediterranean Sea water and heat budgets simulated by an ensemble of high-resolution regional climate models. *Clim Dyn* 37:2067–2086
- Sannino G, Herrmann M, Carillo A, Rupolo V, Ruggiero V, Artale V, Heimbach P (2009) An eddy-permitting model of the Mediterranean Sea with a two-way grid refinement at the Strait of Gibraltar. *Ocean Model* 30:56–72
- Somot S, Sevault F, Dequé, M, Crépon M (2008) 21st century climate change scenario for the Mediterranean using a coupled atmosphere—ocean regional climate model. *Glob Planet Change* 63:112–126
- Stanev EV, Le Traon PY, Peneva EL (2000) Sea level variations and their dependency on meteorological and hydrological forcing: analysis of altimeter and surface data for the Black Sea. *J Geophys Res* 105:203–216
- Struglia MV, Mariotti A, Filogrosso A (2004) River discharge into the Mediterranean Sea: climatology and aspects of the observed variability. *J Clim* 17:4740–4751
- Tiedtke M (1989) A comprehensive mass flux scheme for cumulus parameterization in large-scale models. *Mon Weather Rev* 117:1779–1800
- Trigo IF, Grant RB, Davies TD (2002) Climatology of cyclogenesis mechanisms in the Mediterranean. *Mon Weather Rev* 130:549–569
- Ulbrich U, Leckebusch GC, Pinto JG (2009) Extra-tropical cyclones in the present and future climate: a review. *Theor Appl Climatol* 96:117–131
- UNEP (United Nations Environmental Program) (1992) *World atlas of desertification*. Edward Arnold, London
- Valcke S (2006) OASIS3 user guide. PRISM Support Initiative Rep No. 3. CERFACS, Toulouse
- Van Oldenborgh GJ, Philip S, Collins M (2005) El Niño in a changing climate: a multi-model study. *Ocean Sci* 1:81–95
- Van Ulden AP, van Oldenborgh GJ (2006) Large-scale atmospheric circulation biases and changes in global climate model simulations and their importance for climate change in Central Europe. *Atmos Chem Phys* 6:863–881
- Vörösmarty CJ, Fekete B, Tucker BA (1998) River discharge database, Version 1.1 (RivDIS v1.0 supplement). Available through the Institute for the Study of Earth, Oceans, and Space, University of New Hampshire, Durham, NH
- Yu L, Jin X, Weller RA (2008) Multidecade global flux datasets from the Objectively Analyzed Air–Sea Fluxes (OAFlux) Project: latent and sensible heat fluxes, ocean evaporation, and related surface meteorological variables. OAFlux Project Tech Rep OA-2008-01, Woods Hole Oceanographic Institution, Woods Hole, MA
- Zeng X, Zhao M, Dickinson RE (1998) Intercomparison of bulk aerodynamic algorithms for the computation of sea surface fluxes using TOGA COARE and TAO data. *J Clim* 11:2628–2644

Submitted: February 28, 2011; Accepted: July 25, 2011

Proofs received from author(s): February 13, 2012